Journal of Energy Storage 152 (2026) 120084

Contents lists available at ScienceDirect

Journal of Energy Storage

journal homepage: www.elsevier.com/locate/est

Research Papers

Evaluating densification effects on sulfide-based electrolytes to examine an application in scalable solid-state battery manufacturing

Carina Amata Heck [a,b,*], Duc Hien Nguyen [c], Lars Bröcker [d], Martin Alexander Lange [e], Vasiliki Faka [f], Alexander Diener [a,b], Jeff Bastian Wongso Wijaya [c], Lennart Blume [a,b], Wolfgang G. Zeier [e,f], Bettina V. Lotsch [c], Arno Kwade [a,b], Peter Michalowski [a,b]

[a] Institute for Particle Technology, Technische Universität Braunschweig, 38104 Braunschweig, Germany
[b] Battery LabFactory Braunschweig, Technische Universität Braunschweig, 38106 Braunschweig, Germany
[c] Max-Planck-Institut für Festkörperforschung, 70569 Stuttgart, Germany
[d] Institute for Surface Technology, Technische Universität Braunschweig, 38108 Braunschweig, Germany
[e] Institute of Energy Materials and Devices (IMD), IMD 4: Helmholtz-Institut Münster Ionics in Energy Storage, Forschungszentrum Jülich GmbH, 48149 Münster, Germany
[f] Institute of Inorganic and Analytical Chemistry, University of Münster, 48149 Münster, Germany

ARTICLE INFO

Keywords:
Solid-state batteries
Sulfide-based electrolytes
Densification
Binder

ABSTRACT

To make solid-state batteries viable for industrial applications, the resulting electrode or separator layers must fulfill specific requirements, including the mechanical stability and consistent product quality. This study systematically investigates the processability of slurry-based separators comprised of β-Li_3PS_4 (LPS) and hydrogenated nitrile butadiene rubber (HNBR) as binder for uniaxial densification. Fabrication and stack pressure, densification temperature, and layer thickness are taken into account. Key properties such as coating density, adhesion strength, hardness, reduced elastic modulus, ionic conductivity and electrochemical cell performance are evaluated. To reveal the impact of binder, the ionic conductivity was also analyzed for the pure electrolyte powder. Distribution of relaxation times (DRT) analysis was applied. Significant differences in the stress-induced strain in the electrolyte crystal lattice that is assumed to improve the charge transfer were identified for the binder-based separators compared to pure electrolyte powder. Also, the fast elastic recovery after compaction, potential binder migration, and the importance of the sample cell transfer for the interpretation of the measured ionic conductivity were analyzed. The latter is also compared to separators containing Li_6PS_5Cl (LPSCl). These findings provide fundamental insights into the densification of sulfide-based electrolytes, especially with regard to the role of the binder, which is necessary for scalable battery production.

1. Introduction

Solid-state batteries are a promising next-generation battery technology, which potentially achieve a higher power density and energy density compared to conventional lithium-ion batteries due to the possibility of bipolar stacking and an application of silicon or lithium metal as anode [1–4]. Sulfide-based electrolytes are of particular interest for solid-state batteries due to their high ionic conductivity and ductility [1,2].

One interesting sulfide-based electrolyte material is Li_3PS_4 (LPS), which is associated with having the highest chemical stability in the Li_2S-P_2S_5 systems [5,6]. The crystalline phase of LPS depends on the temperature: A transformation of the low-temperature γ-phase to the β-phase was reported at 573 K, followed by a transition to the α-phase at 746 K [7]. The high-conducting β-phase is stabilized at a lower temperature by nanostructuring [5,8]. However, according to Yang et al. [9], the γ-phase probably can resist larger stress and strain due to a higher bulk, shear and Young's modulus, as well as Poisson ratio when compared to the β-phase.

Furthermore, one fundamental aspect in the processing of solid-state batteries is the choice of binder. The ideal binder has to fulfill several requirements including high cohesion and adhesion, mechanical and (electro-)chemical stability toward sulfide-based ionic conductors, thermal stability, cost efficiency and low environmental impact. In this

* Corresponding author at: Institute for Particle Technology, Technische Universität Braunschweig, 38104 Braunschweig.
E-mail address: c.heck@tu-braunschweig.de (C.A. Heck).

https://doi.org/10.1016/j.est.2025.120084
Received 20 August 2025; Received in revised form 1 December 2025; Accepted 20 December 2025
Available online 29 January 2026

study, hydrogenated nitrile butadiene rubber (HNBR) was used as binder with relatively low glass transition temperature (T_g) needed for flexible and mechanically stable sheets [10,11]. One study identified HNBR as the mechanically best-performing binder compared to poly-isobutylene, poly(butyl methacrylate), poly(styrene-butadiene-styrene), and poly(styrene-ethylene-butadiene-styrene) for the preparation of slurry-based separators [10]. Moreover, it provides high thermal stability [11]. HNBR is a hydrogenated derivative of NBR, exhibiting enhanced oxidative stability due to the saturation of the C=C double bonds in the polymer backbone [10].

However, a major challenge is the sensitivity of sulfides against moisture, resulting in material degradation and the release of toxic hydrogen sulfide (H_2S), thus complicating production scale-up [2,12,13]. The processing is commonly performed in an inert glovebox atmosphere [14–17] or in a dry room [18–20]. The slurry-based separator is either coated directly onto one electrode or is prepared as a free-standing layer, which can be laminated onto the electrode. However, to realize free-standing separators, a high mechanical stability of the layers is required. One important step here is the densification process, commonly realized by uniaxial compaction [17,21]. Ideally, the separator thickness should be reduced as much as possible to improve the specific energy, while minimizing the internal resistance [22]. Thicknesses of as little as 30 µm have been reported in the literature [22,23]. Besides uniaxial densification, warm isostatic compaction is reported to result in a more homogeneous density distribution [18,24,25]. However, for uniaxial and isostatic compaction only semi-continuous processing can be realized while calendering serves as continuous densification strategy [15,26,27]. In one study [15], LPS and LPSCl separators with HNBR were calendered. Here, LPS separators showed high fragility, thus cannot be easily processed. For the LPSCl, better mechanical stability was achieved but slight deterioration in the specific ionic conductivity for an increase in line load or fabrication pressure was found.

The correlation between fabrication and stack pressure is the focus of many research studies [15,21,28,29]. To gain a better understanding, the following section describes possible events beginning from the compaction of the sample to the measurement of impedance that are also illustrated in Fig. 1:

1. During densification, particle rearrangement, binder migration, fragmentation of agglomerates and particles, introduction of strain, elastic and plastic deformation can take place depending on the applied densification parameters and material composition. In the case of amorphous and glass ceramic material, in contrast to microcrystalline particles, a sintering process of the particles is postulated [28]. Furthermore, based on the Janssen effect, the wall friction affects the vertical pressure during powder compaction that can lead to uneven density distribution [30].
2. After stress release, fast elastic recovery occurs. This could result in interparticular micro-contact losses [15,31,32]. Moreover, different elastic recovery of the individual components can result in cracks within the sample [33].
3. For the analysis of the ionic conductivity after densification, the sample is either measured in the same cell body used for densification or is transferred in a new cell body. This is particularly important because, during densification, the sample is effectively pressed into the surface of the current collectors, ensuring better contact with the current collector when the same cell body is used for electrochemical impedance spectroscopy (EIS). However, in the case of calendering the sample always has to be transferred in a cell body after compaction for EIS, thus cannot be compacted in the cell body itself [15].
4. Interface resistance between the current collector and sample is significantly dependent on the stack pressure likely due to uneven surface roughness resulting in current constrictions [15,21,29]. Recommendations here are to use carbon powder as the current collector to allow better contacting also at low stack pressure [21] or sputtering of noble metals onto the pellet for conformal contact [29].
5. Depending on the compaction state of the sample and applied stack pressure, renewed particle rearrangement, as well as plastic and elastic deformation can take place.

2. Experimental

2.1. General conditions

Unless noted otherwise all processing steps and sample preparations were performed in an argon-gas-filled glovebox (generally $H_20 < 5$ ppm,

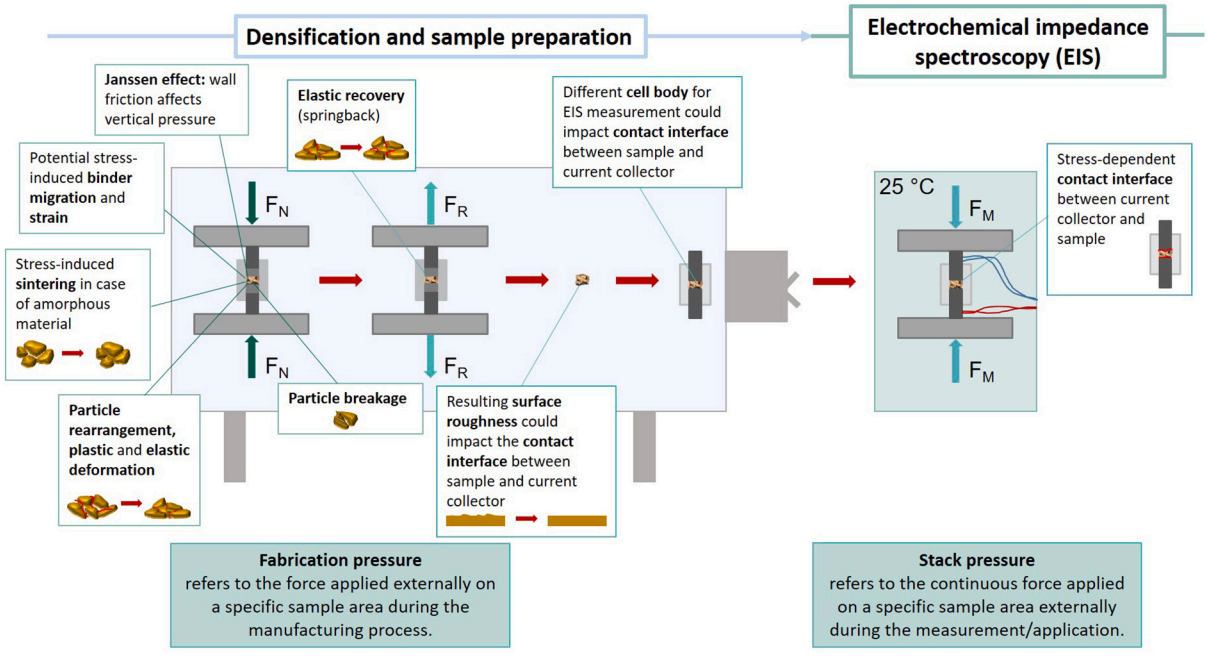

Fig. 1. Schematic illustration of the densification of a separator in a glovebox followed by EIS in a climate chamber.

$O_2 < 5$ ppm).

2.2. Material

Commercial β-LPS (NEI Corporation) was used as solid electrolyte with a particle size distribution of $d_{10} \approx 1$ µm, $d_{50} \approx 7$ µm, and $d_{90} \approx 40$ µm measured by analytical centrifugation as reported in a former study (slight underestimation of coarser particles possible due to premature sedimentation) [15]. Particles with a diameter of up to 100 µm are present. The tested LPSCl (NEI Corporation) has a particle size distribution of $d_{10} \approx 1$ µm, $d_{50} \approx 2$ µm, and $d_{90} \approx 7$ µm [15]. At a stack pressure of 25 MPa and 25 °C and a pre-compaction at 100 MPa and 40 °C an ionic conductivity of 0.02 mS cm^{-1} was measured for LPS and 1.18 mS cm^{-1} for LPSCl (see Figs. 4 and 6). To produce slurry-based layers, p-xylene (Merck KGaA) was used as the solvent and HNBR (Therban AT LT 2004, Arlanxeo Deutschland GmbH) as the binder. To allow good analysis of the separators, the slurry was coated onto aluminum foil in case of LPS (Speira GmbH) and in case of LPSCl onto a siliconized polyester foil (PPI Adhesive Products GmbH).

2.3. Separator preparation

For this study, separators with 97 wt% or 95.7 wt% solid electrolyte and, accordingly, 3 wt% or 4.3 wt% HNBR binder were produced. HNBR was first dissolved in p-xylene, followed by adding the electrolyte powder. Using a dissolver (Dispermat CV3-PLUS, VMA Getzmann GmbH), a peripheral disk velocity of 1 m s^{-1} was kept for 30 min to reach a 30 wt% solids content, before being increased to 3 m s^{-1} for another 60 min. The slurry was coated onto an aluminum substrate by a film applicator (Coatmaster 510, Erichsen GmbH & Co. KG) with a coating speed of 10 mm s^{-1} at room temperature. Aluminum was used as substrate since the LPS-based sheets are not mechanically stable enough to form a free-standing film. Two layer thicknesses were investigated by producing sheets with 300 µm (S_{300}) and 500 µm (S_{500}) gap of the doctor blade (see Table 1). Afterwards, the separators were dried overnight at room temperature. Additionally, analogous to the LPS separators, LPSCl separators were produced with 95.7 wt% electrolyte and 4.3 wt% HNBR binder but with a solids content of 63.5 wt% and were coated onto a siliconized foil.

2.4. Densification

Uniaxial densification was realized using a two-column laboratory press (PW 10, Paul-Otto Weber GmbH). For the binder-based separators, samples were punched out. For the pure electrolyte samples, ca. 150 mg of electrolyte powder was used for the compaction. All samples were left either in a heatable pressing matrix or transferred into a cell body consisting of a PTFE cylinder and two stainless steel plungers for 2 min for acclimatization followed by another 2 min for the compaction. The thickness of the separator were determined using a tactile dial gauge (Mitutoyo). The mass was weighed using a fine balance (Sartorius Lab Instruments GmbH & Co. KG). For LPS and HNBR, respectively, true densities of 1.88 g cm^{-3} [34] and 0.96 g cm^{-3} [15] were used. Presuming that the materials are inert towards each other, and that the binder is homogeneously distributed, the density of the solid electrolyte and binder mixture ρ_M can be calculated to be 1.83 g cm^{-3} for a 3 wt% binder content, and 1.81 g cm^{-3} for a 4.3 wt% binder content. For the determination of the coating density, the thickness and weight of three to five samples were measured. The rate of compression was calculated according to Eq. (1) with δ_a being the layer thickness after densification and δ_i being the initial layer thickness in a non-compacted state: [35].

$$\Pi = 1 - \frac{\delta_a}{\delta_i} \tag{1}$$

2.5. Adhesion/cohesion strength measurement

Adhesion/cohesion strength was measured according to Haselrieder et al. [36] with a material testing device (Z020, ZwickRoell GmbH & Co. KG). For standardization, punched-out separator samples with a diameter of 12 mm were measured. The measurements were realized in a dry room with an air supply dew point of $T_D \approx -27$ °C.

2.6. Pore size distribution

The pore size distributions of the separators were measured by mercury intrusion (Quantachrome Instruments) according to the procedure of Froboese et al. [37]

2.7. Scanning electron microscopy (SEM)

SEM images were obtained in an SEM Phenom XL (Thermo Fisher Scientific Inc.) at 0.1 Pa and a primary beam voltage of 10 kV/15 kV. The device is placed in a dry room (air supply dew point $T_D \approx -27$ °C). Energy-dispersive X-ray spectroscopy (EDX) mapping was performed with a Crossbeam 340 (Carl Zeiss Microscopy Deutschland GmbH) at 10 kV.

2.8. Electrochemical impedance spectroscopy (EIS)

For EIS, the separator was placed between two sealed stainless steel plungers in an air-tight PTFE tube [14,15,38]. The samples were removed from the glovebox and kept for 20 min in a climate chamber (SU-242, ESPEC) at 25 °C for acclimatization. The measurement was performed using a potentiostat (Zennium, Zahner-Elektrik GmbH & Co. KG) with a frequency range of 4 MHz to 10 Hz in potentiostatic mode with an amplitude of 20 mV. Stack pressure was applied either by a cell press at 25 MPa or by a manual hydraulic press (MP250D, MAASSEN

Table 1
Definition of the separator types described in this study.

Separator type	Description	Schematic illustration	Solid electrolyte	Binder content
S_{300}	The slurry was coated by a 300 µm gap size of the doctor blade onto the substrate.	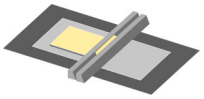	LPS	3 wt%
S_{500}	The slurry was coated by a 500 µm gap size of the doctor blade onto the substrate.	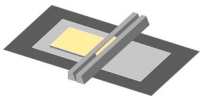	LPS LPSCl	3 wt%/ 4.3 wt% 4.3 wt%
Pure powder	Pellet consisting of electrolyte powder.		LPS LPSCl	0 wt% 0 wt%

GmbH) for stack pressures >25 MPa. Relaxis 3 (rhd instruments GmbH & Co. KG) was used for data analysis. The Kramers-Kronig relations to identify the reliable frequency range for data fitting assessed the data quality.

2.9. Distribution of relaxation times (DRT) analysis

Prior to DRT analysis, all spectra were corrected for their open-circuit high-frequency offset verified for physically meaningful behavior. The processed data were then loaded into a Python environment (Python 3.13.5) with the *hybrid-drt* package from Huang et al. [39] installed. DRT inversion was performed using the packages probabilistic hybrid regression-classification framework, yielding the distribution of relaxation time $\gamma(\tau)$ over log-spaced relaxation timescales τ. This probabilistic output reflects the hybrid regression–classification framework proposed by Huang et al. [39] For each spectrum, the dual-inversion algorithm was applied to generate and compare candidate discrete equivalent-circuit–like models, selecting the most plausible representation based on internal scoring metrics. The identification and robustness of characteristic relaxation times were confirmed by evaluating and comparing three independent impedance spectra for each material under identical conditions.

2.10. Nanoindentation

Nanoindentation was performed using a TriboIndenter TI 900 (Hysitron Inc.). The samples were prepared on a glass slide in a glovebox. The measurement was performed under a constant argon-gas flow. Global measurement was performed by stressing the samples with a flat punch ($\varnothing = 50$ µm). For the reduced elastic modulus, the deformation of the diamond tip is included but estimated as negligible. The device software provided the data for hardness and reduced elastic modulus.

2.11. X-ray diffraction (XRD)

A Stoe StadiP powder diffractometer in Debye Scherrer geometry with Mo Kα_1 radiation ($\lambda = 0.7093$ Å) was utilized for X-ray diffraction measurements. The 2θ collection ranged from 4° to 60°, with a step size of 0.015°. To avoid material degradation in air, samples were sealed in borosilicate glass capillaries.

2.12. Rietveld analysis and Stephens anisotropic microstrain model analysis

Rietveld refinements were carried out using the TOPAS-Academic V7.25 software package [40]. Structural information of LPS was taken from Homma et al. [7] An instrumental parameter file was created by refining a LaB_6 standard. The peak shape was modeled using a modified Thomson−Cox−Hastings pseudo-Voigt function, which was refined to the peak shape of the LaB_6 standard. For the subsequent refinements, U, X, and Y were constrained to instrument values and W was refined freely [41]. Fit indicators (e.g., R_{wp} and R_{exp}) were used to assess the quality of the refined structural models. The obtained goodness-of-fits resulted mostly in values above 2 due to the high statistics of the measurement and thus very low R_{exp}. The following parameters were initially refined: (1) scale factor, (2) background coefficients using a Chebyshev function with 12 free parameters, (3) zero-shift error, (4) the peak shape parameter W of the initially obtained modified Thomson−Cox − Hastings pseudo-Voigt function modeled peak shape, (5) lattice parameters, (6) fractional atomic coordinates, (7) isotropic atomic displacement parameters, (8) atomic occupancies of the anions. The latter ones were then allowed to refine subsequently with all other parameters, to quantify the anion site disorder. In the final step, Stephens' anisotropic strain model was used to describe the internal strain, since significant anisotropic peak broadening was observed in the strained samples [42]. The model allows for six independent strain parameters in a cubic system, S400, S040, S004, S220, S202 and S022 corresponding to the axis direction and surface diagonals of the orthorhombic unit cell of LPS. Resulting values were plotted according to the generalized mustrain approach from GSAS II as strain-surface plots [43].

2.13. Fourier-transform infrared (FTIR) spectroscopy

FTIR spectroscopy measurements in the ATR (attenuated total reflection) mode were performed in ambient atmosphere using a Nicolet iS 50 FTIR system (Thermo Fisher Scientific Inc.), equipped with an MCT detector, a SMART iTX ATR accessory and a germanium crystal. The angle of incidence was 45° and 64 scans were accumulated at a spectral resolution of 4 cm^{-1}. Before each series of measurements, a background spectrum was taken and before each FTIR-ATR measurement, the Ge crystal was cleaned with ethanol. Separator samples were quickly pressed onto the cleaned Ge crystal to minimize reactions of the electrolyte with ambient water vapor as much as possible.

In order to analyze a possible accumulation of the binder at the separator surface the SpectraRay/4 software for simulation of optical ellipsometry, absorption and transmission from Sentech Instruments GmbH was used to calculate ATR absorbances due to vibrations of aliphatic -CH_2- near 2900 cm^{-1} of the pure binder and of LPS/binder composites, respectively.

2.14. Measurements with CompreDrive

For the LPS powder, ~100 mg or less was loaded into the CompreCell of the CompreDrive (rhd instruments GmbH & Co. KG), an electrochemical test system with controllable pressure application. For the binder-based sheets, two punched out discs were stacked systematically in the CompreCell, pre-pressed at around 100 MPa for 10 min to remove the aluminum foil, because contact points between the aluminum and electrolyte-binder layer were broken resulting in a single disc being loaded back into the CompreCell. The CompreCell is equipped with two hard tungsten carbide pistons with a diameter of 6 mm, which serve as electrodes and apply uniaxial force to the sample. Double O-rings within the cell maintain an air-tight seal, ensuring an inert atmosphere during the experiment.

Once the sample was loaded, the cell was transferred out of the glovebox and mounted in a CompreDrive press, which was connected to a potentiostat (NEISYS novocontrol) in a two-electrode configuration. The CompreDrive press, controlled by CompreDriveControl software (ver. 1.15), allows for real-time monitoring of applied force and precise stack pressure control. The software also tracks motor position, enabling the calculation of the relative piston displacement at any given time.

A reference blank cell measurement was conducted before to determine the reference motor position for every relevant pressure step. This reference was later used to adjust for setup deformation by subtracting the reference motor positions from the sample measurements, allowing the calculation of the in situ sample thickness. Temperature control was achieved with a Julabo Presto A40 thermostat, which was connected to a heating/cooling mantle surrounding the cell.

EIS was employed to measure the ionic conductivity of the samples. Measurements were performed at stack pressures of 0.01, 0.025, 0.05, 0.1, 0.2, 0.3, 0.4, 0.5, 0.6, 0.7, 0.8, 0.9, 1.0, 1.1, 1.2, 1.3, 1.4, and 1.5 GPa during the compression cycle, followed by decompression in the reverse order. A resting time of 15 min was adjusted between each stack pressure step to ensure pressure equilibration. Impedance spectra were recorded at 25 °C, across a frequency range from 1 MHz to 1 Hz, with an applied AC voltage of 25 mV (rms). Data were analyzed using RelaxIS 3 software (rhd instruments GmbH & Co. KG), applying proportional weighting to the data points. The frequency range was adjusted to 1 MHz to 1 kHz for some samples to ensure meaningful fits. Following the EIS measurements, the cell was reintroduced into the glovebox, where the samples were then removed from the CompreCell to record their final weights and thicknesses.

2.15. Measurement of elastic recovery

In order to estimate the elastic recovery of the separators after compaction, a material testing device (Z020, ZwickRoell GmbH & Co. KG) was used placed in a dry room (air supply dew point $T_D \approx -27$ °C). Both plungers for supporting the sample and compaction (∅ = 1 mm of the upper plunger) are made of hardened steel (hardness = 1620 ± 50 kg mm^{-2}). Elastic recovery was tested at two different speeds, 1 mm min^{-1} and 5 mm min^{-1} (loading speed = unloading speed). For compaction, 500 N was set (≈640 MPa). To account for the recovery of the measurement setup itself, linear regression was conducted for five unloading force-displacement curves for each tested speed (see Fig. S1 in the Supporting Information), and the averaged slope was used as correction factor a_{corr} to obtain the corrected plunger distance $d_{p,corr}$ according to Eq. (2):

$$d_{p,corr} = d_p + \frac{F}{a_{corr}} \tag{2}$$

The recovery was calculated as described in Eq. (3) with δ_a being the separator thickness after compaction and δ_{max} being the separator thickness at maximum load:

$$Springback = \frac{\delta_a - \delta_{max}}{\delta_{max}} \bullet 100\% \tag{3}$$

To determine δ_a, the corrected plunger distance was identified for the loss of plunger contact to the separator sample and for δ_{max} the corrected plunger distance at maximum load.

2.16. Estimation of statistical significance

To estimate the statistical significance of the measurement data in terms of nanoindentation and elastic recovery using a two-tailed Welch's *t*-test, the *p*-value was calculated according to Eq. (4):

$$p = 2^*(1 - F(|t|)) \tag{4}$$

F(|t|) denotes the cumulative distribution function of the test statistic distribution under the null hypothesis. A p-value <0.05 indicates that the probability of obtaining such an extreme result, assuming the null hypothesis of no statistical difference in the measurement data is true, is less than 5 %. This argues against the null hypothesis and provides evidence of a real effect or difference in the data.

2.17. Electrochemical characterization

Rate performing tests were conducted using a BaSyTec XCTS (BaSyTec GmbH) in a climate chamber (Binder GmbH) at 25 °C and a stack pressure of 25 MPa. The cells were cycled in a voltage window of 2.2 V to 3.7 V vs. Li/InLi. The applied charge and discharge rates were varied from 0.02C (CCCV, 3 cycles), 0.05C (CCCV, 3 cycles), 0.1C (CCCV, 3 cycles) and 0.02C (CCCV, 1 cycle). Indium (99.99 %, 127 µm thickness, Thermo Fisher Scientific Inc.) served as the anode with a diameter of 12 mm. Cathodes were used with 71 wt% single-crystalline $LiNi_{0.83}Mn_{0.06}Co_{0.11}O_2$ (MSE Supplies LLC) as cathode active material, 24 wt% LPSCl (pre-milled), 3 wt% polyisobutylene (Oppanol N80, BASF SE) and 2 wt% carbon black (C-NERGY Super C65, Imerys S. A.). For the cathode slurry preparation by dissolving (Dispermat CV3-PLUS, VMA-Getzmann GmbH) p-xylene was used as solvent. The solids content was 35 wt% and the peripheral velocity of the disk 4 m s^{-1} for 60 min. The slurry was coated onto aluminum (Coatmaster 510, Erichsen GmbH & Co. Kg, 10 mm s^{-1}). The separator was coated directly onto the dried cathode also by doctor blading with a gap size of 500 µm. The mass load of the cathode was 9 ± 1 mg cm^{-2}. The cathode-separator composite with a diameter of 15 mm was compacted at 200 MPa and 40 °C for 2 min after 2 min acclimatization. Due to the direct coating of the cathode with the separator, the exact mass of the cathode samples used for cell assembly could not be directly determined and was therefore estimated using cathode samples without the separator.

3. Results and discussion

3.1. Adhesion/cohesion strength, reduced modulus of elasticity, and layer hardness

In order to investigate the densification of the LPS separators, the impact of fabrication pressure and temperature were analyzed. One of the first observations when dealing with LPS separators is that they become brittle in the compacted state. Low fracture toughness despite the low material stiffness is already described for 70:30 Li_2S-P_2S_5 [44]. The LPS layers become more brittle with increasing fabrication pressure. Moreover, a curvature of the samples after fabrication gets more pronounced until a fabrication pressure of 200 MPa, while 300 MPa samples are flat after densification and partly or entirely detached from the substrate (Fig. 2a)). The curvature observed after densification may result from the high stress at the interface between the substrate and electrolyte layer, due to the greater lateral strain, thus stretching the electrolyte layer more than the aluminum substrate [45]. At 300 MPa, this stress may be sufficient to disrupt the contacts between the substrate and electrolyte layer, leading to partial or entire detachment of the electrolyte layer from the substrate [45]. This is also reflected in the adhesion/cohesion strength measured for a fabrication pressure of 25 MPa to 400 MPa shown in Fig. 2b). In the non-compacted state, a cohesive failure was observed, where only the upper layer of the separator peeled off, resulting in the measurement of a very low cohesion strength of 0.13 MPa. However, an adhesive failure was observed for all compacted samples. The entire layer detached from the aluminum substrate. The densification results in an initial increase of the adhesion strength for densification pressures of 50 MPa and 100 MPa, followed by a decrease for fabrication pressures of 300 MPa and 400 MPa probably due to the reduction of contact area between the coating layer and the tested aluminum. As mentioned before, samples compacted at 200 MPa showed a strong curvature. For testing, the samples must be placed flat onto a stamp; they need to be straightened, resulting in additional stress on the separator leading to strong flaking, hindering a measurement of samples compacted at 200 MPa. For 300 MPa and 400 MPa, the adhesion strength decrease is also accompanied with higher standard deviation due to the high brittleness and partial detachment of the electrolyte layer resulting in random cracking and flaking.

In Fig. 2c) the resulting adhesion strength is shown as a function of the densification temperature from 20 °C to 100 °C compacted at 100 MPa (adhesive failure) compared to the non-compacted state (cohesive failure). An increase in the temperature results in a linear increase in the adhesion strength for the observed temperature range. For the separators compacted at 100 °C, the highest adhesion strength of 1.27 MPa was measured. The strength increase probably results from the softening of the viscoelastic binder leading to a higher amount of contact points between the particles and substrate. In addition, after compaction and cooling to room temperature, potential shrinkage of the binder takes place, creating additional tension and improving the adhesion strength to the substrate. In real battery cell applications, the separator is coated or laminated onto the electrode. Based on these results, better adhesion can also be expected for high temperature application during the densification of the electrode-separator compound.

Fig. 2d) demonstrates the reduced elastic modulus obtained by nanoindentation. It is increased when going from a non-compacted state to 100 MPa and to 300 MPa. Thus, a denser structure of the separators results in a higher resistance against deformation, and increased material stiffness. A slight increase in the reduced elastic modulus was observed for the separator compacted at 100 °C compared to 40 °C (*p*-value = 0.036 according to Eq. (4)). The layer's hardness (Fig. 2e)) increased when going from a non-compacted state to 100 MPa and 300 MPa due to increased interlocking of the sulfidic particles (see Fig. S9 in the Supporting Information). Moreover, the hardness of the

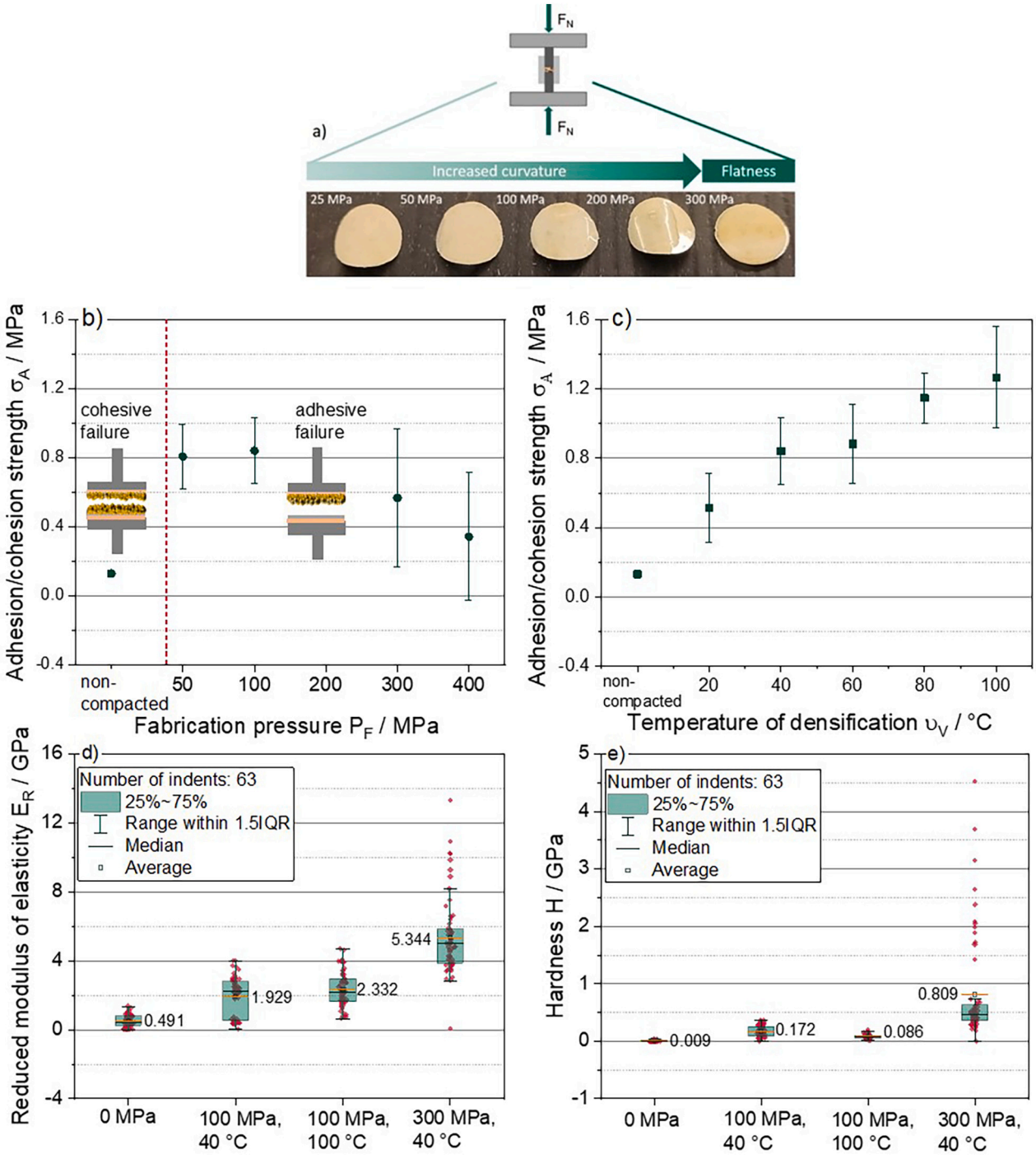

Fig. 2. a) Schematic illustration of the uniaxial compaction adapted from Heck et al., Ref. [15] under the terms of the CC-BY 4.0 license. Copyright: The Authors (2024), published by Wiley-VCH GmbH and LPS separators compacted with different fabrication pressures. b) Adhesion/cohesion strength as a function of the fabrication pressure of separators S_{300} compacted at 40 °C. Error bars present the standard deviation of ten samples. c) Adhesion strength as a function of the densification temperature of separators S_{300} compacted at 100 MPa. Error bars present the standard deviation of nine to ten samples. d) Reduced elastic modulus for different densification states determined by 63 indents. e) Hardness for different densification states determined by 63 indents. Individual data points are shown as red dots, the average value is shown in numbers. All graphs present data for LPS separators with 3 wt% HNBR. (For interpretation of the references to colour in this figure legend, the reader is referred to the web version of this article.)

separator compacted at 100 °C is lower compared to the samples compacted at 40 °C (p-value = 4.85 •10^{-9} according to Eq. (4)). Reduced hardness at 100 °C might be caused by a thermal softening of the electrolyte and/or binder and plasticizing effects of the electrolyte. Similar to the adhesion/cohesion strength, the spread of the measurement data at 300 MPa for both hardness and reduced elastic modulus is very high as it is typical for brittle materials [46].

3.2. Separator surface

In Fig. 3a) SEM images are shown for separator S_{300} and S_{500} samples non-compacted and compacted. The densification temperature was 40 °C. The higher the fabrication pressure, the smoother the surface appears. The separator surface roughness influences the contacting with the electrodes. For example, in the case of lithium metal, rough surface

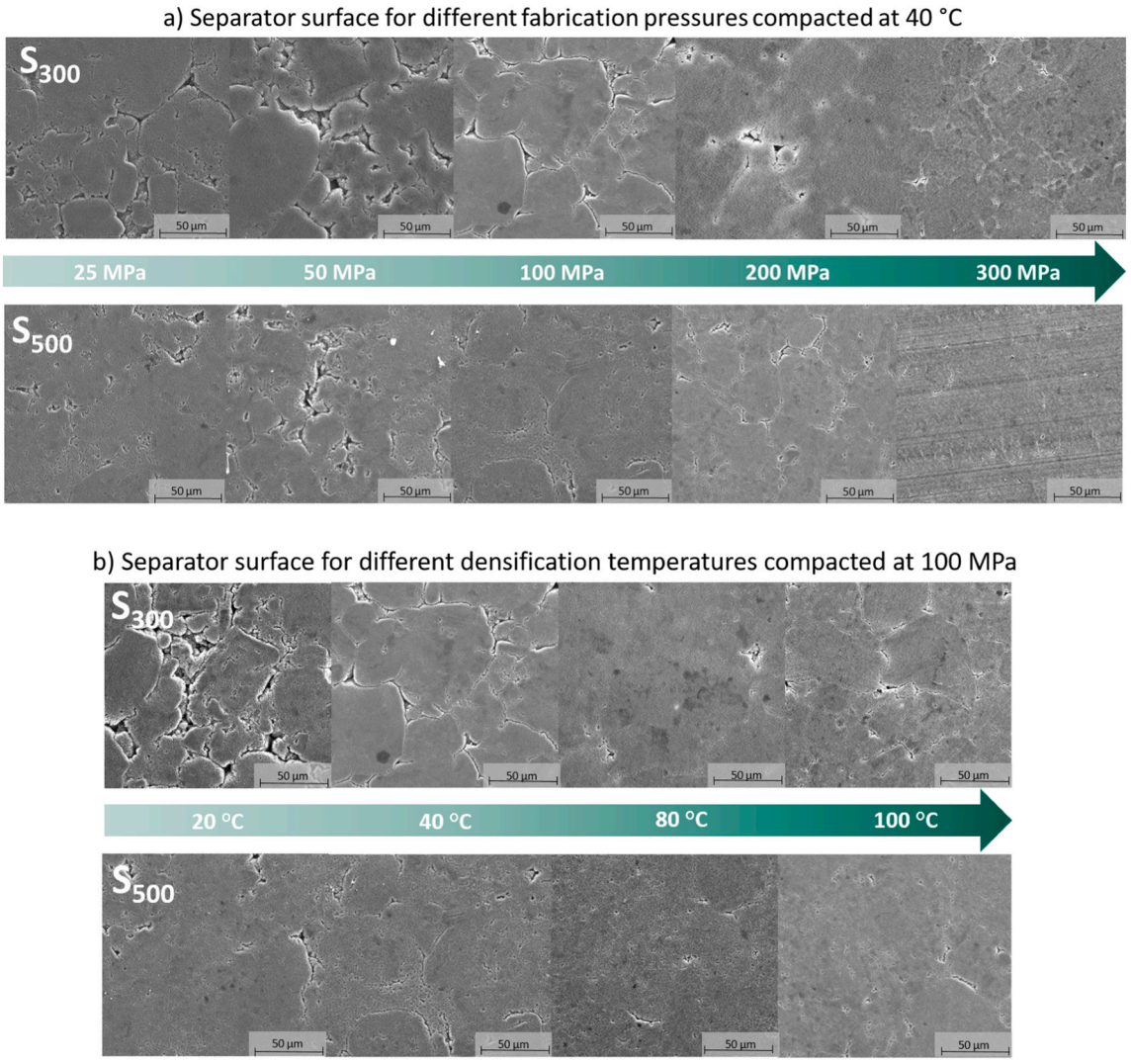

Fig. 3. SEM images of separator S_{300} and S_{500} layers with 3 wt% HNBR for a) different fabrication pressures (compacted at 40 °C) and b) different densification temperatures (compacted at 100 MPa).

structure of the separator favors short circuits due to the current focusing on sharper protrusions [47]. In Fig. 3b) SEM images of the separator surface compacted at different densification temperatures but with a constant pressure of 100 MPa are shown. An increased sintering of the particles can be observed for separator S_{300} when going from 20 °C to 40 °C to 80 °C. In contrast, according to the areas depicted for SEM analysis no significant difference for the different densification temperatures can be seen for separator S_{500}. Close particle contact on the separator surface is already achieved at 20 °C. It is presumed that the reduction of surface roughness also affects the contact with the current collector for impedance measurement.

3.3. *Specific ionic conductivity – Impact of fabrication pressure on LPS*

In order to investigate the impact of the separator surface for different fabrication pressures on the results of impedance measurement the following analyses were conducted: In Fig. 4b) to d) the ionic conductivity of the pure powder and separators with 3 wt% and 4.3 wt% binder as a function of the fabrication pressure is shown. Representative Nyquist plots and used equivalent circuits are shown in Figs. S2 and S3 in the Supporting Information. The samples either were measured right after compaction in the cell body that also was used for the compaction (press body = cell body) or were compacted and measured in two different bodies (press body ≠ cell body, see Fig. 4a)).

In the first case, the separator was compacted and EIS was measured in the same PTFE cell body. In the second case, the separator was compacted in a stainless steel pressing matrix and transferred into a PTFE cell body with stainless steel plungers. For the pure powder, the ionic conductivity is slightly higher for samples that are compacted in the same body for a fabrication pressure >25 MPa. This is due to the better contact with the plungers used as current collector and thus, reduced contact resistance between the plungers and the sample. Additionally, the stress exerted on the separator can slightly vary between the PTFE cell and the stainless steel pressing matrix, even if the same force is applied due to the individual wall friction effects of the cell material used according to the well-known Janssen equation [30].

For 3 wt% and 4.3 wt% HNBR, also generally a higher ionic conductivity was measured for the samples directly compacted in the cell body. However, for the pure powder the trend in ionic conductivity remains for both cell transfer systems (increase in ionic conductivity with an increase in fabrication pressure). Instead, for 4.3 wt%, the ionic conductivity rather increases in case of press body = cell body while it rather remains on a constant level for press body ≠ cell body. This may be attributed to different surface roughness after densification for samples with binder compared to the pure powder: The binder can act as a filler between the electrolyte particles, closing voids and thus,

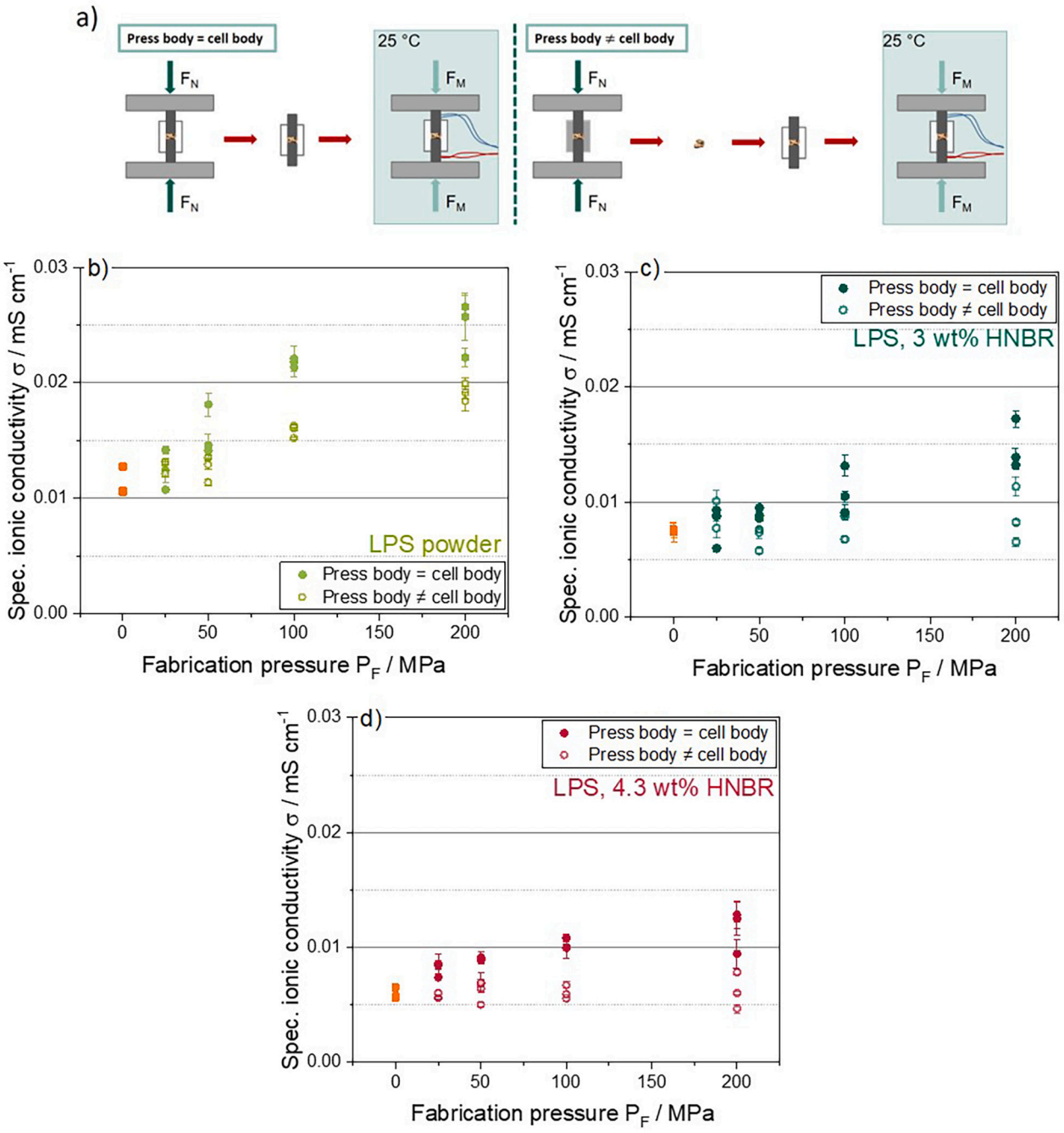

Fig. 4. a) Schematic illustration of press body = cell body and press body ≠ cell body. Specific ionic conductivity as a function of the fabrication pressure for separators with b) pure LPS powder, c) 3 wt% HNBR and d) 4.3 wt% HNBR of separator S_{500}. The orange data points present the non-compacted samples. All measurements were performed at 25 °C and a stack pressure of 25 MPa. Each data point represents one individual sample measured. For each variation, three samples were measured, in exceptional cases two. The standard deviation is based on the variation of the layer thickness and the fit error given by RelaxIS.

smoothing the surface. In addition, the binder-based separators were coated onto aluminum. The surface characteristics of the measurement plungers are also expected to influence the measurement results.

Additionally, DRT analysis was performed. The results are shown in Fig. 5. The peaks were assigned based on reference [48]. Bulk transport is not visible, since the corresponding time constant is not possible to resolve within the measured frequency range. The pure LPS powder shows the highest grain boundary contribution which gets smaller with binder addition and shifted to lower time constants (= faster process) for more binder (Fig. 5a)). Thus, the introduction of the HNBR reduces the grain boundary contributions significantly probably due to a surface passivation of the LPS particles. The pure LPS shows a facilitation in grain boundary contribution (faster process at lower time constant) with densification (Fig. 5b)). For the LPS separators with 3 wt% HNBR there is a more pronounced facilitation with compaction. Compaction in the cell body itself shifts the grain boundary contribution to lower time constants than for press body ≠ cell body. Separators with 4.3 wt% HNBR exhibit less of a shift with applied pressure. Compaction in the cell body shifts the process to lower time constants but for press body ≠ cell body the potential two processes do not get faster but less pronounced, relatively the slower process gets even more weight.

These findings imply that for the LPS high fabrication pressure is needed to improve the ionic conductivity. If possible, the sample should be compacted in the cell body itself for EIS analysis.

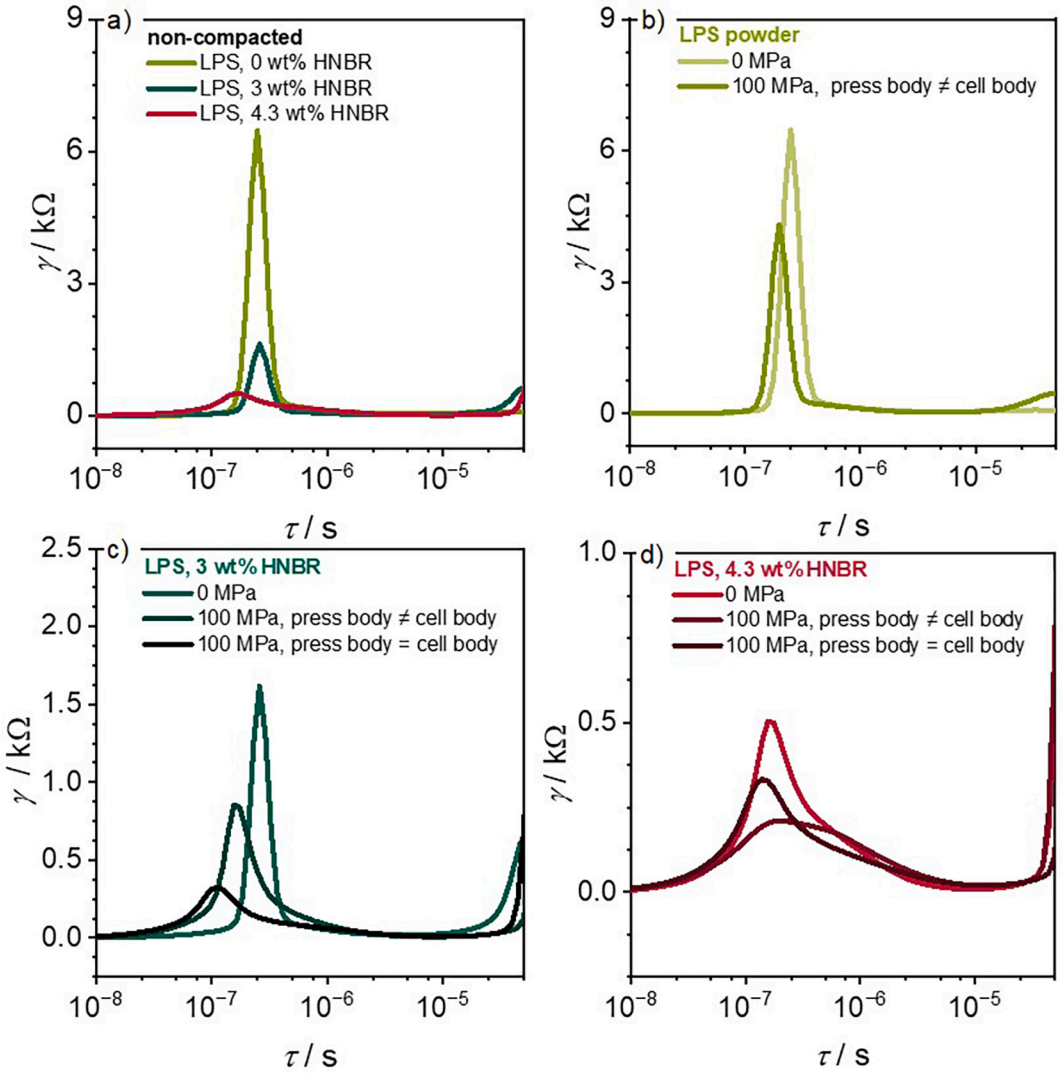

Fig. 5. a) Results of DRT analysis for separators with pure powder, 3 wt% and 4.3 wt% HNBR. Results of DRT analysis for b) the pure LPS powder, c) separator with 3 wt% HNBR and d) 4.3 wt% HNBR for non-compacted state and compacted at 100 MPa for press body = cell body and press body ≠ cell body. EIS was performed at 25 °C and a stack pressure of 25 MPa.

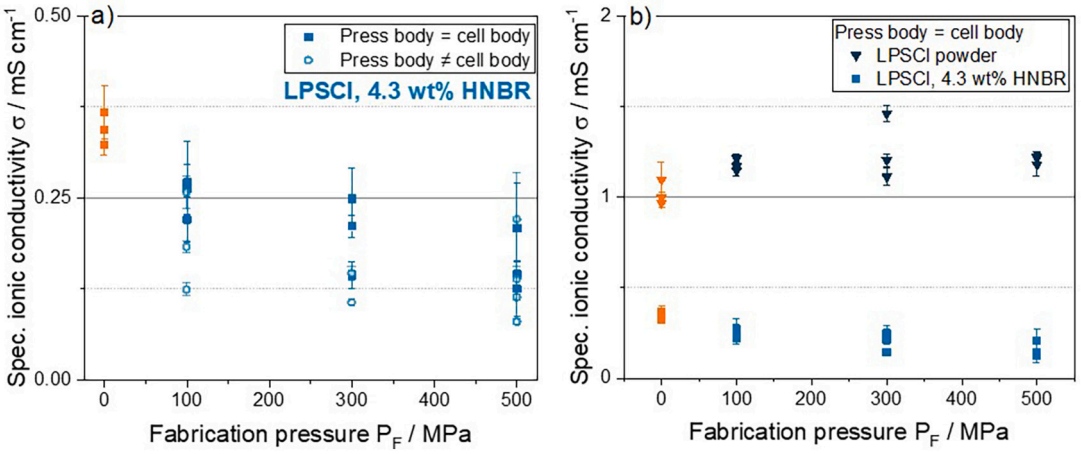

Fig. 6. Specific ionic conductivity as a function of the fabrication pressure for separators with a) LPSCl and 4.3 wt% HNBR analyzed for press body = cell body and press body ≠ cell body and b) for LPSCl and 4.3 wt% HNBR compared to pure LPSCl powder compacted in press body = cell body. The orange data points present the non-compacted samples. All measurements were performed at 25 °C and a stack pressure of 25 MPa. Each data point represents one individual sample measured. For each variation, data points of three samples measured are shown, in exceptional case two or four. The standard deviation is based on the variation of the layer thickness and the fit error given by RelaxIS.

3.4. Specific ionic conductivity – Impact of fabrication pressure on LPSCl

In order to compare these findings with another electrolyte, the results of a former study [15] for LPSCl were reproduced (press body ≠ cell body) compared to samples compacted in the same body (press body = cell body, Fig. 6a)). In contrast to the results obtained for LPS the ionic conductivity decreases for both cell setups with an increase in fabrication pressure. Different dependencies on the fabrication and stack pressure for different sulfide-based electrolytes are already reported by Cronau et al. [28] They postulate a difference in the compaction results for amorphous and crystalline materials: While pressure-induced sintering is expected to occur in amorphous material, the grain boundaries between crystalline particles are still preserved after pressure release [28]. Cross-section SEM images shown in S7 to S11 confirm a sintering of LPS after compaction, while for the LPSCl no sintering effect appears. LPS is a less crystalline and softer material compared to LPSCl [49,50]. In case of pure powder demonstrated by Cronau et al. [28], despite the potential absence of particle sintering in microcrystalline electrolytes, an increase in ionic conductivity with increase in fabrication pressure was observed at stack pressures above 50 MPa. However, a former study [15] demonstrated that even at a high stack pressure of 70 MPa (contact resistance is assumed to be negligible for 70 MPa based on the results obtained by Doux et al. [21]) the densified LPSCl-HNBR separators exhibit lower conductivity compared to the non-compacted ones. The fact that the reduced ionic conductivity in compacted state originates from the HNBR and not from the absence of a sintering effect is additionally supported by the increase in the ionic conductivity for the pure LPSCl powder in compacted state compared to the non-compacted state (see Fig. 6b)).

The different results for LPS and LPSCl separator compaction might be explained by a different binder distribution and/or resulting porosity due to the different solids contents realized by dispersion process. For the LPSCl a higher solids content (63.5 wt%) for the same binder content can be realized compared to LPS (30 wt%) due to viscosity limitations. Literature findings also indicate that this type of LPS in combination with HNBR allows only low solids contents [14,38], while LPSCl slurries can be formulated with substantially higher solids contents [10,15,32]. This might be due to the high porosity of the LPS particles themselves presumably due to synthesis conditions (see Fig. S4 in the Supporting Information) resulting in a high specific surface area. Due to the higher solids content for LPSCl, the non-compacted separator has a lower porosity (37 ± 2 %) compared to the non-compacted LPS separator (76 ± 4 %) [15]. Possibly, for the compaction of the highly porous LPS separator the particle-particle contact is significantly improved while for the LPSCl separator compaction results in a more insulating embedding in the HNBR binder. Another reason might be different particle rearrangement due to different particle sizes. If large particles are present relative to the layer thickness, as is the case with LPS in this study, the deformation behavior of the separator is influenced sooner by the direct compression of the particles than by their rearrangement. In addition, the impact of fast elastic recovery after compaction should be addressed in future studies [15,32].

In terms of ionic conductivity, these findings imply that no compaction should be performed for LPSCl-HNBR separators (at least for the tested binder content of 4.3 wt%). No significant difference in the measured ionic conductivity was found whether the sample was compacted in the cell body or not.

3.5. Specific ionic conductivity – Impact of stack pressure on LPS

An increase in the stack pressure led to an increase in the ionic conductivity of the binder-based LPS separators (Fig. 7). Similar ionic conductivities were obtained for stack pressures at 25 MPa, 50 MPa, 100 MPa and 200 MPa for 3 wt% and 4.3 wt% binder-based separators. This indicates that the insulating character of the binder is limiting the ionic transportation at higher stack pressures, while for lower stack pressures voids are more relevant (see Fig. 8a)). Moreover, besides the denser structure of the sample the contact resistance to the current collector (plungers of the cell body) decreases with increasing stack pressure, resulting in the measurement of a higher ionic conductivity [21].

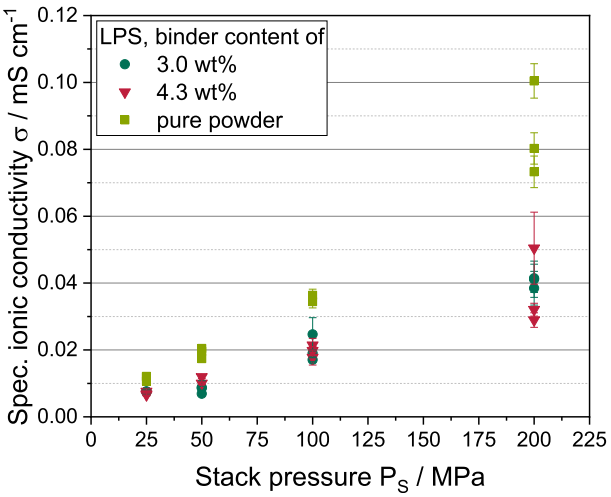

Fig. 7. Specific ionic conductivity of separator S_{500} with a binder content of 3 wt% and 4.3 wt% and pure LPS powder as a function of the stack pressure. Each data point presents one individual sample measured. For each variation, data points of three samples are shown, in exceptional case two. The standard deviation is based on the variation of the layer thickness and the fit error given by RelaxIS. All measurements were performed at 25 °C.

In order to investigate the impact of stack pressure in more detail, the ionic conductivity was also measured as a function of the applied stack pressure from 0.01 GPa to 1.5 GPa and its release back to 0.01 GPa for the pure LPS powder, as well as separators with 3 wt% and 4.3 wt% binder content (Fig. 8a)). One measurement series is based on the stepwise compaction and subsequent stress release of one sample in contrast to the results presented in Fig. 7. In Fig. 7, each data point represents the measurement of a single individual sample, being measured only once. For the stepwise increase of stack pressure in Fig. 8 in case of pure powder, a maximum ionic conductivity of 0.26 mS cm^{-1} at 1.3 GPa was achieved, for 3 wt% HNBR 0.09 mS cm^{-1} at 1.2 GPa and for 4.3 wt% 0.08 mS cm^{-1} at 1.3 GPa. The measured ionic conductivity is consistent with the given ionic conductivity by the LPS manufacturer between 10^{-4} und 10^{-5} S cm^{-1} and data from literature [14,51,52].

For the pure LPS powder also a second compaction and pressure release was applied (see Fig. 8b)). A lower ionic conductivity was achieved compared to the first compaction but results in a similar ionic conductivity at 0.1 GPa with 0.14 mS cm^{-1} (first compaction) and 0.13 mS cm^{-1} (second compaction) [29].

XRD for the pure powder is exemplarily shown in Fig. 8c), in-situ high-pressure X-ray synchrotron diffraction data and the corresponding Rietveld refinement for the LPS powder and the separators with 3 wt % and 4.3 wt% HNBR are presented in Fig. S5 and S6 in the Supporting Information, as well as the crystallographic information in Table S1 to S5. For all XRD refinements, LPS crystallization in the metastable β-phase with 2 wt% Li_2S is confirmed. The strain analysis reveals that the LPS material is already slightly strained (1 %) in the non-compacted state, likely due to synthesis conditions and slight anisotropy (more strain along the short unit cell axis in [010] and [001] direction, significant strain in [101] and [011] direction).

This is enhanced by compaction to 1.5 GPa for all samples: The strain in diagonal direction [101] and [011] outweighs the axis, but there is no significant strain in [100] and [110] direction. This is in agreement with previous work, where strain is induced in the Li_6PS_5Br argyrodite pressed within the same pressure range [53]. The strain increases from

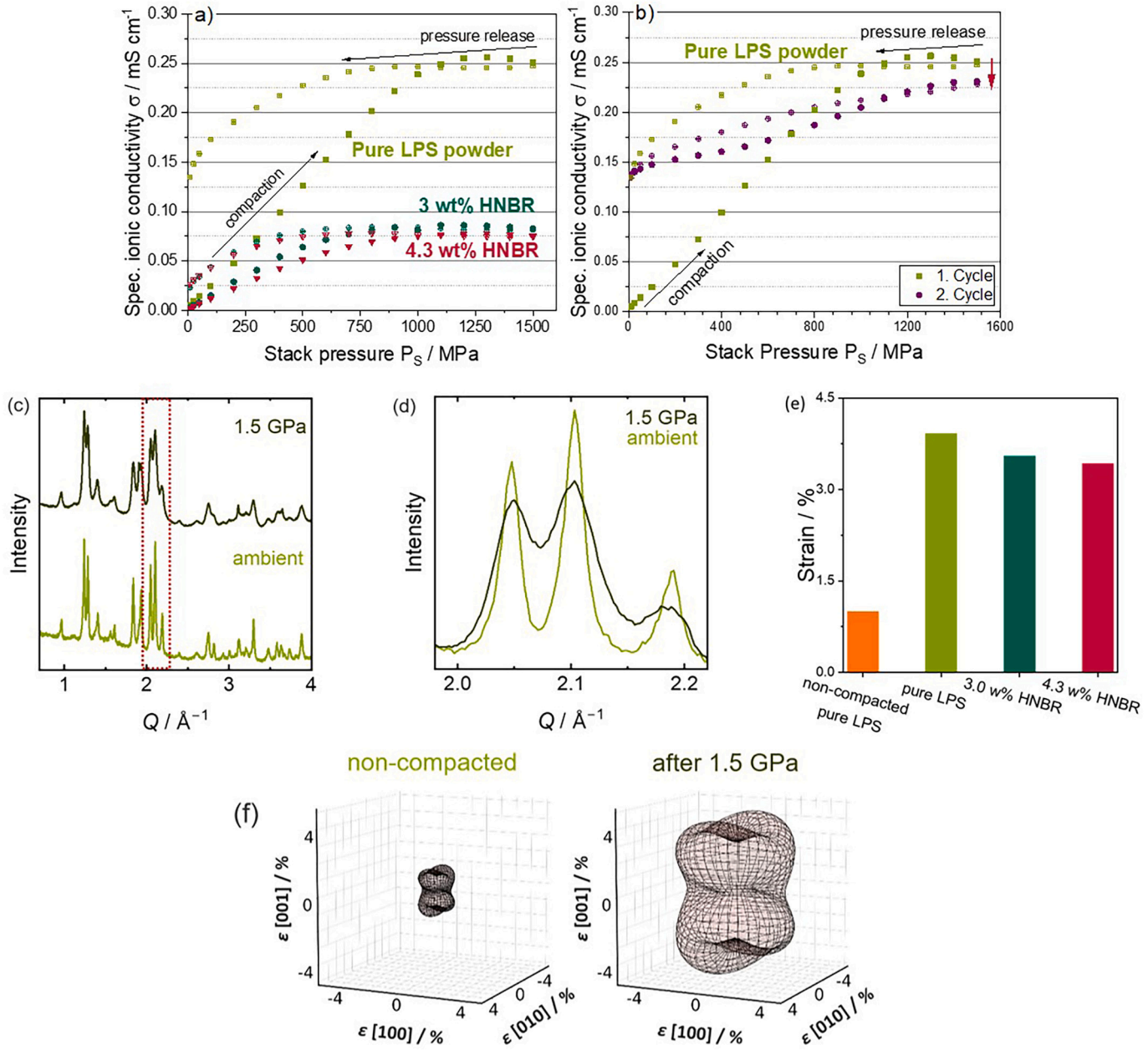

Fig. 8. Specific ionic conductivity of a) separators with 3 wt% and 4.3 wt% binder, as well as pure LPS powder and b) for two compaction cycles of the pure LPS powder. Each data point represents an average of three measurements; the second cycle for the LPS powder is based on one measurement. The unfilled points represent the progression of pressure release. The measurements were performed at 25 °C and a stepwise increase of the stack pressure applied to the sample. The error bars include the fitting errors of the impedance measurements as well as the measurement error of the CompreDrive. c) and d) X-ray diffraction patterns of the LPS powder before and after compaction at 1.5 GPa. e) Generalized microstrain for the LPS powder non-compacted and after compaction at 1.5 GPa, as well as separators with 3 wt% and 4.3 wt% binder after compaction at 1.5 GPa and f) corresponding strain contour plots of the LPS powder.

1 % to 3.9 % for the pure LPS powder, but the presence of binder significantly reduces the straining of the material for the same pressure to 3.6 % for 3 wt% HNBR and 3.4 % for 4.3 wt% HNBR. The strain describes the introduction of lattice defects, e. g. dislocations, facilitating charge transport and thus, improves ionic conductivity [53]. Consequently, it can be hypothesized that the binder acts as a buffer during compaction reducing the amount of strain. Thus, ionic conductivity for the binder-based samples is lower compared to samples compacted without binder not only because of its insulating property but also due to the reduction of stress-induced strain.

3.6. Layer thickness, coating density, and pore size distribution

Fig. 9a) presents the layer thickness as a function of the rate of compression for two different initial layer thicknesses (S_{300}, ~131 µm, S_{500}, ~308 µm) and a densification temperature of 40 °C and 100 °C. The initial layer thickness of separator S_{300} is 57 % smaller compared to S_{500}. For separator S_{300} a minimum thickness of 42 µm was achieved compared to 102 µm for separator S_{500}, both for a densification at 300 MPa and 100 °C. To achieve a low area-specific resistance and an energy density that is sufficient for an industrial solid-state battery production a separator thickness below 20 µm is required [22]. However, LPS-based separators are probably too fragile to further reduce the separator thickness.

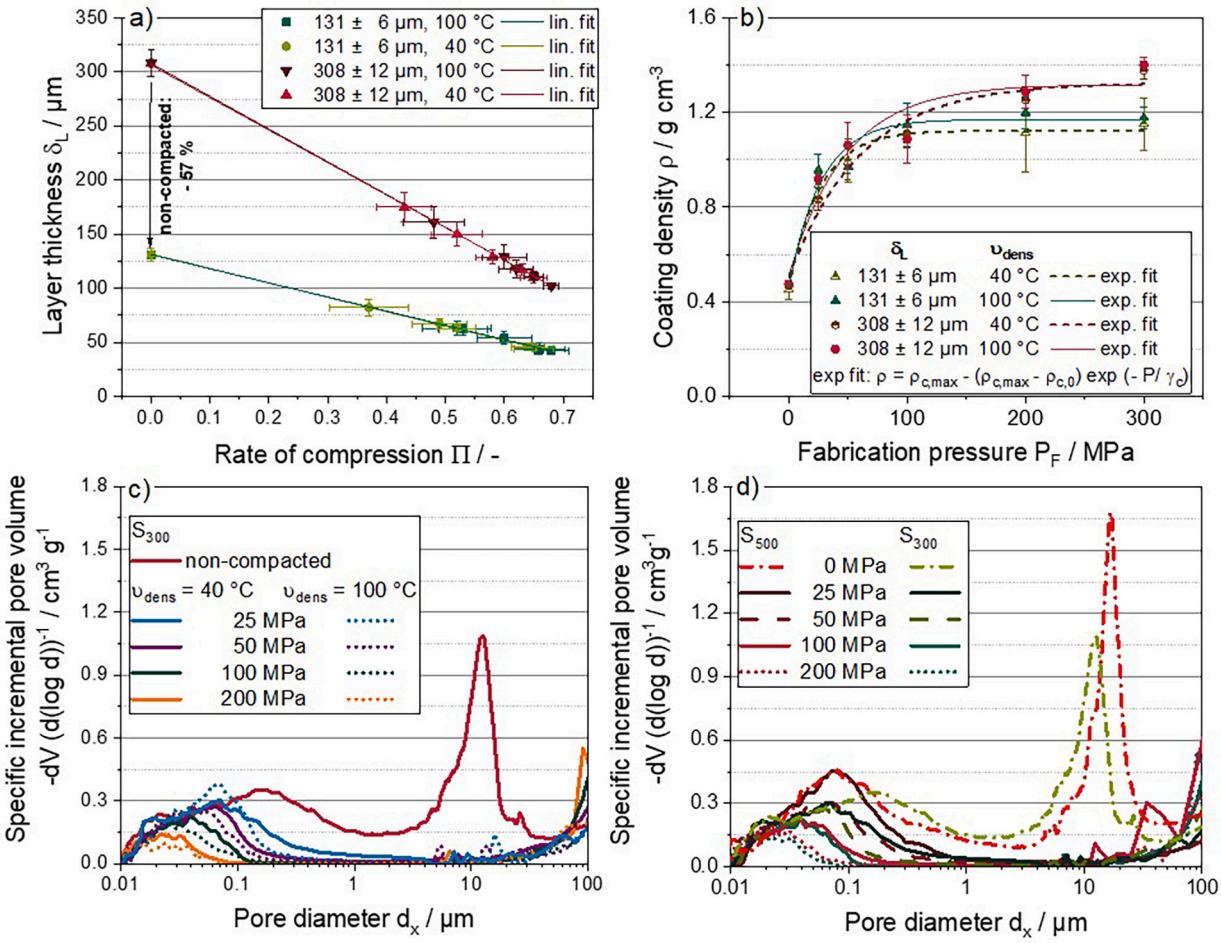

Fig. 9. a) Layer thickness as a function of the rate of compression. Error bars represent the standard deviation of 15 to 25 layer thickness values for each variation. b) Density as a function of the fabrication pressure. Error bars represent the standard deviation of the calculated density of three to five samples. Exponential fit according to C. Meyer et al. was applied [54]. c) Pore size distribution of separator S_{300}. The separators were compacted at 40 °C or 100 °C. d) Pore size distribution of separators S_{300} and S_{500}. All graphs present data for LPS separators with 3 wt% HNBR.

In Fig. 9b) the coating density as a function of the fabrication pressure and densification temperature is shown for two different layer thicknesses. Meyer et al. [54] developed an exponential approximation based on the Heckel's equation [55] to quantify the compaction resistance (see Eq. (5)):

$$\rho_c = \rho_{c,max} - (\rho_{c,max} - \rho_{c,0}) \exp\left(-\frac{P}{\gamma_c}\right) \quad (5)$$

ρ_c denotes the coating density, $\rho_{c,max}$ the maximum coating density, $\rho_{c,0}$ the initial coating density, P the applied pressure and γ_c the compaction resistance. The approximation parameters are listed in Table S6 in the Supporting Information.

As already shown for conventional electrodes [45,56,57] the compaction resistance γ_c increases with an increase in the mass loading. This is attributed to a higher interparticular friction due to the higher amount of particles [45,57]. The thinner layers show a lower maximum density compared to the thicker ones [15,57,56]. Reasons are a weaker effect of the more porous contact layers at the dies on the overall density, as well as stronger particle rearrangement takes place in the thicker layer [15,56]. In general, a slightly higher density for the same densification pressure was measured for 100 °C compared to 40 °C likely due to a higher plasticity of the binder. However, due to the variability indicated by the standard deviation, no conclusive interpretation is possible. The glass transition temperature T_g of LPS is ~200 °C [34]. Here, a relative density of 98 % at 270 MPa for pure LPS powder is described [34]. The reduction of porosity and the increased particle sintering with an increase in fabrication pressure might be the main reasons for the increased brittleness of the layers because pores act as stress focal points within the porous layer, providing higher flexibility, and facilitating elastic recovery. Higher porosity for thinner layers conflicts with the overall goal of producing thin separators (<20 µm in the compacted state), which are known to result in low internal resistance, high energy density, and reduced battery cell weight [47]. In Fig. 9c) the pore size distribution of compacted separator S_{300} samples is shown as determined by mercury intrusion [37]. As expected, the pore size within the separator decrease with increasing fabrication pressure. It has to be noted that only accessible pores can be measured by mercury intrusion [37]. A densification pressure of 25 MPa can already significantly reduce the pore size in comparison to the non-compacted state. Furthermore, densification at 100 °C in comparison to 40 °C at a pressure of 25 MPa and 50 MPa results in a slight shift of the pore size distribution to smaller pore size.

Fig. 9d) demonstrates the pore size distribution obtained for separators S_{300} and S_{500}. The pore size distribution is slightly shifted for 25 MPa, 50 MPa, 100 MPa and 200 MPa to smaller pore sizes for the separators S_{300} compared to S_{500}. For thinner layers, evaporation usually occurs more uniformly due to the shorter transport paths for solvent removal probably affecting the resulting pore size. The smaller pore size of the thinner layer due to the solvent evaporation effects seems to be preserved even after compaction. However, edge effects and measurement artefacts should be considered, such as pores near the separator

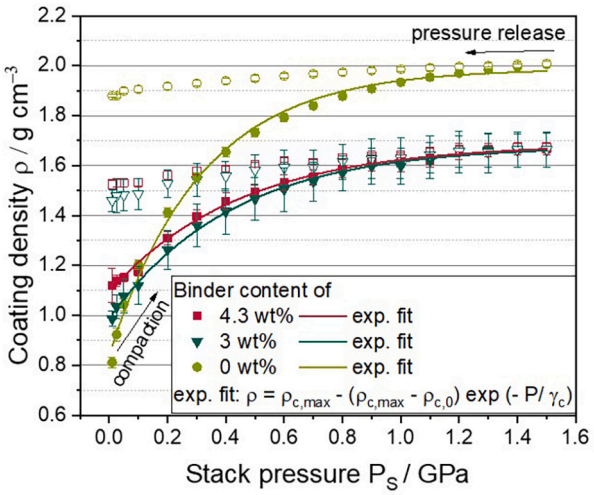

Fig. 10. Density as a function of the stack pressure for pure LPS powder and separator sheets with 3 wt% and 4.3 wt% binder under "in die" measurement conditions. Exponential fit according to C. Meyer et al. was applied [54]. Before each measurement series, the samples with HNBR were pre-compacted at 100 MPa for 10 min to detach the aluminum substrate. The open points represent the progression of pressure release. The measurements were performed at 25 °C with increasing stack pressure applied to the sample. Error bars represent the standard deviation of the calculated density of three samples for each variation.

surface have a greater influence on the result obtained for the thinner layers. Also, pores at the lateral surface of the samples have a higher impact onto the measurement result for the thicker layer.

Fig. 10 depicts the relation between density and stack pressure for pure LPS powder, as well as for separators containing 3 wt% and 4.3 wt % HNBR (in relation to the measurements of ionic conductivity shown in Fig. 8). For each variation, three measurements were conducted and averaged. The separators with HNBR (two S_{500} separators) were pre-compacted at 100 MPa for 10 min in order to detach the aluminum substrate as preliminary tests have demonstrated that the substrate affects the measurement results. The measurement procedure includes stepwise compaction of a sample from 0.01 GPa to 1.5 GPa without intermediate pressure release, followed by a stepwise pressure release back to 0.01 GPa. This is called "in die" measurement condition with in situ determination of the sample thickness while for the results in Fig. 9 b) "out of die" measurements were performed [29,58]. For Fig. 9b), each sample was compacted only once and the thickness was measured after pressure release (effects like elastic recovery took place). For the LPS powder a density of 2 g cm^{-3} was measured at 1.5 GPa. In Table S7 the initial and maximum coating density at a pressure of 0.1 GPa, and the compaction resistance are listed for each measurement estimated according to Eq. (5) [54]. Here, the initial coating density is increased from pure powder to 3 wt% to 4.3 wt% binder content. This is due to the pre-compaction of the samples with HNBR, the filler effect of the binder, and better cohesion between the particles resulting in a denser structure.

However, the maximum coating density of the electrolyte material without binder is higher than that of the samples with HNBR binder. Due to the lower true density of the binder, the compound density is lower compared to the true density of the pure powder. In samples with HNBR binder, small voids often remain because the binder, even under high pressure, does not fully collapse due to its elasticity. This elasticity allows the binder to maintain a certain level of volume, preventing it from being completely compacted like the harder sulfidic particles. These small voids act as buffers within the structure, maintaining some level of porosity. Due to its buffer character, the HNBR also absorbs part of the stresses, probably reducing the deformation of the sulfide-based particles and induced strain in the LPS material (see Fig. 8). Additionally, a slight further increase in the density can be expected for a further increase in the applied pressure >1.5 GPa, meaning that the maximum achievable density may not be reached. The compaction resistance for the pure LPS powder is lower compared to the samples with binder resulting from the higher elastic resistance of the binder, reduced degree of motion of the LPS particles embedded in the binder matrix and lack of pre-compaction.

3.7. Particle fragmentation

SEM images of separator cross-sections are shown in Fig. S7. Here, particle fragmentation can be assumed for densification at both low (20 °C) and high (100 °C) temperatures compacted at 100 MPa but cannot be clearly distinguished from sintered grain boundaries. The porous LPS particles (Fig. S4) possess inherent fracture points which may further break apart during compaction. Particle breakage due to compaction has already been reported for harder materials such as secondary cathode active materials [59,60], as well as for LPS (in a composite cathode) [60] and LPSCl [15] as electrolyte material. However, in composites the stress is concentrated more strongly on the material with high Young's modulus [61]. Particle breakage probably results in additional interfacial resistance and affects the possible achievable maximum density. Apart from this, an increased moisture uptake after calendering is described for conventional electrodes due to an increased surface area caused by particle breakage of the active material and elastic recovery [59,62]. Whether this also applies to the moisture-sensitive electrolyte has to be evaluated. Also, small particles are more likely to be pressed into voids and particle strength increases with a decrease in particle size [15,63–65].

3.8. Considerations on binder migration by FTIR-ATR analysis

Fig. 11a) shows the results of FTIR-ATR measurements of separator samples, produced with different fabrication pressures and with 4.3 wt% binder content. Additionally, Table S8 in the Supporting Information summarizes the positions of dominant peaks in the binder spectrum. Peak positions due to LPS or products of its superficial hydrolysis are not listed in Table S8 [66].

The binder material is similar to so-called grafted HXNBR (hydrogenated carboxyl nitrile rubber) [67]. Here, grafted XNBR (carboxyl nitrile rubber) was synthesized by esterification between carboxyl groups (-COOH) of XNBR and alkanols or glycols with different molecular weights. Afterwards, the material was hydrogenated. Strong signals of aliphatic -CH_2-, very similar to polyethylene, can be seen at 2926 cm^{-1}, 2855 cm^{-1}, 1464 cm^{-1}, and 723 cm^{-1} belonging to asymmetric and symmetric stretching vibrations of C-H, deformation vibrations of C-H and C-C rocking vibrations, respectively. The peak of the nitrile group can be found at 2236 cm^{-1}. Oxygen-containing moieties are visible at 1730 cm^{-1}, namely the stretching vibration of C=O, and around 1171 cm^{-1}, where several bands of C-O-C stretching vibrations in esters overlap.

The modeled layer system consists of an n,k layer for the Ge crystal with $n_{Ge} = 4$, $k_{Ge} = 0$ [68], an ultrathin oscillator layer for the binder, applying data for polyethylene (PE) from Ref. [68], because PE is structurally similar to the (-CH_2-)$_n$ domains of the used binder material, and an effective medium layer for the LPS/pore(air)/binder composite. For LPS, an n,k model was used with an average over crystal directions of $n_{LPS} = 2.14$ and $k_{LPS} = 0$ [69]. Using densities of 1.85 g cm^{-3} for LPS and 0.96 g cm^{-3} for HNBR, volume fractions required for optical simulation can be calculated: Assuming an air-pore fraction of 40 vol%, and 4.3 wt% binder in the mixture with LPS, the volume fraction of binder in the final composite is ~4.7 vol%.

Fig. 11b) shows simulated -CH_2- signals near 2900 cm^{-1} for the composite only and for the composite with additional ultrathin binder layers at the separator surface. The black curve for a 10 µm layer, representing virtually pure HNBR (black line in Fig. 11 a)), was normalized

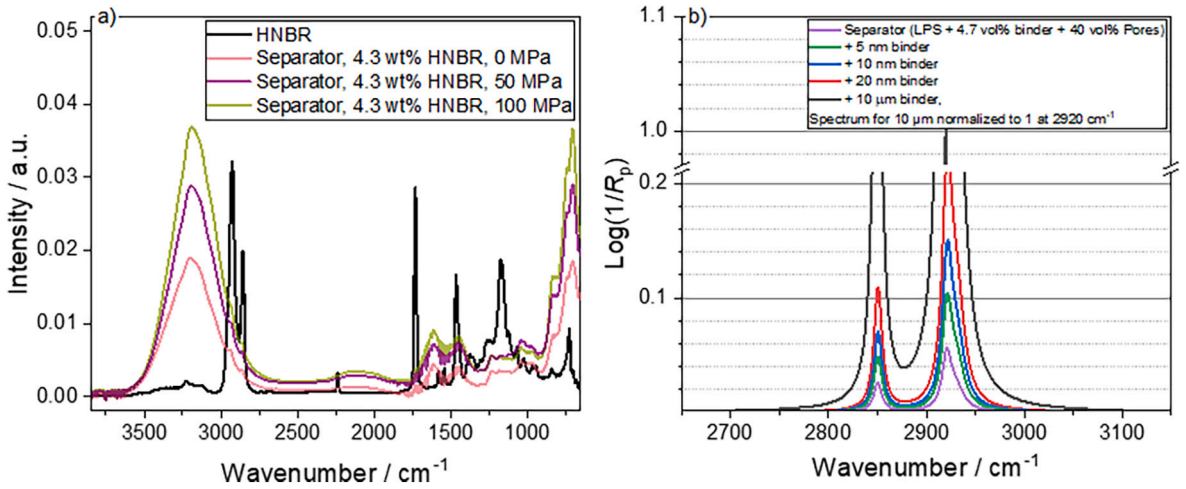

Fig. 11. a) Representative FTIR spectra of binder material (black line) and separator samples produced with different fabrication pressures and 4.3 wt% HNBR. b) Simulations of the absorbance of peaks belonging to the asymmetric and symmetric stretching vibrations of -CH_2-. Purple curve: theoretical IR signal for LPS separator samples with 4.3 wt% binder (4.7 vol%) and 40 vol% pores. All other curves have a thin binder layer with different thicknesses at the surface. (For interpretation of the references to colour in this figure legend, the reader is referred to the web version of this article.)

to 1 at 2920 cm^{-1} and all other graphs were multiplied with the same scaling factor. According to the calculations, 5.5 % of the absorbance of pure HNBR should be found experimentally for the composite. An additional uniform 5 nm HNBR layer on top should raise the absorbance to 10.5 % of the pure binder absorbance.

Experimentally, three spectra each were analyzed for densification pressures of 0 MPa, 50 MPa and 100 MPa, and values for the relative binder absorbance were averaged, resulting in 4.6 ± 0.3 % for 0 MPa, 5.2 ± 0.1 % for 50 MPa and 4.9 ± 0.2 % for 100 MPa fabrication pressure. These values are on average 10 % below the result calculated without superficial 5 nm binder film (5.5 %), see Fig. 11 b). Moreover, there is no significant increase of the relative binder absorbance with increasing fabrication pressure, which could be assumed if an accumulation of HNBR were the reason for a decreasing specific ionic conductivity for higher pressures. Therefore, it is quite unlikely that a thin binder film on the separator surface is formed by densification. It should be noted that weaker infrared signals often result in an increase in densification degree due to reduced penetration depth. However, since the presumed polymer layer is extremely thin, it is fully probed by the IR beam, ensuring that the –CH_2 signals are accurately detected.

For further validation, EDX-mapping of non-compacted and at 100 MPa compacted LPS (and LPSCl separators) with 4.3 wt% binder were performed. In addition, no clear evidence for a binder migration to the surface of the separators caused by compaction was found. The nitrogen signal, used as a marker for the HNBR binder, was evaluated but was generally quite low. The SEM images and corresponding EDX line mapping are shown in Fig. S8 to S11 in the Supporting Information. For final conclusions, Time-of-Flight Secondary Ion Mass Spectrometry Profiling (ToF-SIMS Profiling) should be performed.

3.9. Estimation of fast elastic recovery

The springback for separators with a binder content of 3 wt% and 4.3 wt% was exemplarily measured directly after stress release for two different loading speeds (loading speed = unloading speed) of 1 mm min^{-1} and 5 mm min^{-1} at a load of approximately 640 MPa. The results are shown in Fig. 12. The springback increases for both an increase in binder content (*p*-value of 10 • 10^{-6} for 1 mm min^{-1} and 2 • 10^{-3} for 5 mm min^{-1}), as well as an increase in loading speed (p-value of 4 • 10^{-11} for 3 wt% and 2 • 10^{-6} for 4.3 wt%).

For 3 wt% HNBR, the separator thickness recovers by 6.7 % on average for 1 mm min^{-1}, and 9.2 % for 5 mm min^{-1}. For 4.3 wt% HNBR,

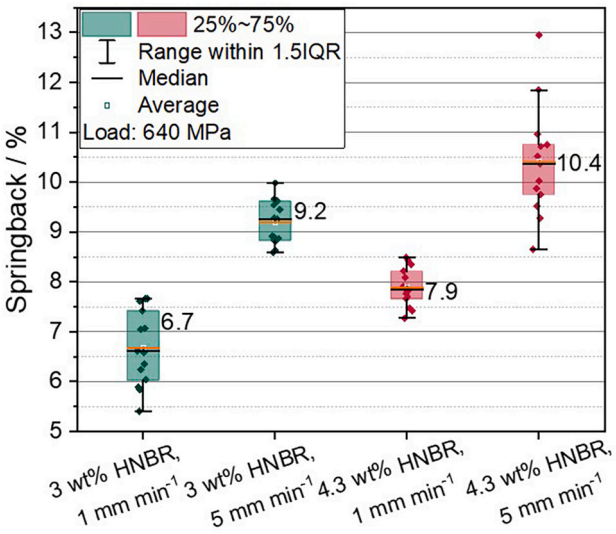

Fig. 12. Estimated springback for separators with a binder content of 3 wt% and 4.3 wt% and an un-/loading speed of 1 mm min^{-1} compared to 5 mm min^{-1}. For each variation 13 to 15 measurements were performed. Individual data point are shown, the average value is shown in numbers.

the springback increases from 7.9 % to 10.4 % on average for an increase in the loading speed. The higher springback for a higher binder content confirms that the binder contributes more to the elasticity and flexibility of the separator layer compared to the sulfide-based particles. In addition, the binder acts as a buffer. With an increase in the HNBR amount, stress absorption by the binder is enhanced and thus, plastic deformation of the particles is minimized. Consequently, the partly elastic recovery of the binder embedding the sulfide-based particles might result in a reinforcement of inhomogeneous density distribution in case of non-ideal binder distribution, formation of cavities and thus, microscopic contact loss between the electrolyte particles. If the cohesion of the electrolyte particles within the separator layer are deteriorated after densification, ionic conductivity can probably be negatively affected [15,32]. As it is already hypothesized for tabling, the different elastic recovery of the electrolyte and binder could result in high local stress and thus, microcracks [33]. For HNBR, the elasticity and thus, springback can be reduced by increasing the content of the polar acrylonitrile

[70]. However, the requirement of a low springback to minimize a potential negative impact on the microstructure may conflict with a sufficiently high flexibility and mechanical stability of the separator. Moreover, the springback is decreased for a decrease in loading speed. This is probably mainly due to the binder's viscoelastic behavior. During fast loading, viscous effects are less strong, and elastic behavior dominates. From this point of view, slow and stepwise pressure application and release are recommended to reduce the impact of elastic recovery and the achievement of a higher density. In addition, elastic recovery is expected to mostly occur directly after densification while slight recovery occurs during long-term retention of the separator. Short-term inert storage is not expected to significantly alter the recovery behavior. For HNBR, the dominant portion of the rebound occurs immediately after unloading, driven by its elastic component. Any additional recovery during subsequent inert storage would be limited to minor viscoelastic relaxation processes and is typically small in magnitude. Elastic recovery was quantified only in the vertical direction, although minor recovery is expected in the lateral directions as well. In order to investigate the specific effect of the springback onto the microstructure, in-situ SEM or micro-computed tomography (μCT) measurements should be applied before and after compaction in future studies.

3.10. Rate performance

In Fig. 13 the specific discharge capacity of rate performance testing is shown for half cells with LPS separators (3 wt% HNBR) in comparison to separators composed of pure LPS powder. The binder-based separator was directly coated onto the cathode. Higher specific discharge capacity at 0.02C was achieved for the pure LPS powder. However, for 0.05C and 0.1C slightly higher discharge capacity was achieved for the cells with binder-containing separators (relatively high standard deviation should be considered). This might be due to thinner layer thickness realized for the binder-based separators compared to the powder-based separators. In addition, at the cathode-separator interface slight degradation of the LPSCl in the composite cathode could be expected due to electrochemical side reactions between the LPSCl, the conductive additive and HNBR [71]. The performance data indicates that the separator design has a substantial impact on the cell performance of the solid-state battery.

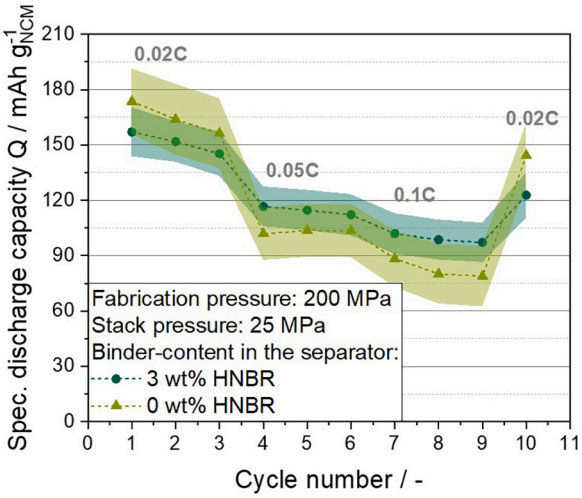

Fig. 13. Specific discharge capacity of rate performance test of half-cells with separators containing 3 wt% HNBR and separators composed of pure LPS powder (0 wt% HNBR) at 25 °C and a stack pressure of 25 MPa. The cathode-separator compound was compacted at 200 MPa. Error bars represent the standard deviation based on the performance data of four half-cells tested.

3.11. Evaluation in terms of scalable separator manufacturing

A binder is essential for the scalable production of solid-state separators because it provides the mechanical cohesion and structural integrity needed during fabrication, especially for thin separator layers <20 μm. The electrolyte powder alone cannot be cast, laminated, or roll-processed by calendering in a stable and defect-free form without a component that holds the electrolyte particles together. In this study, HNBR was tested for slurry-based separator production due to high mechanical stability of the produced separators reported in literature [10]. However, the HNBR binder significantly reduces the ionic conductivity not only by its insulating character but also because the stress-induced strain in the electrolyte is minimized. In case of LPSCl-HNBR separators, the conductivity was actually reduced in compacted state.

Lower binder content results in a lower elastic recovery. Thus, the binder amount should be reduced to an absolute minimum. Isostatic pressing could facilitate this more efficiently, given that calendering necessitates highly mechanically robust layers. However, slow stress release and roller circumferential speed, respectively, necessary to reduce the elastic recovery after densification contrasts industrial-relevant high-speed throughput. In terms of EIS analysis, appropriate measurement strategies have to be established for industrial relevant calendering to be able to measure the effectiveness of densification because the sample cannot be directly compacted in the cell body (compare Fig. 4).

In terms of the electrolyte, LPS is in contrast to LPSCl not suitable for scale-up processing due to its high brittleness and lower ionic conductivity. The high fragility results in a high product rejection rate and reduced reproducibility. However, the phenomenon of reduced ionic conductivity for the binder-containing LPSCl separators in compacted state should be further investigated. For example, these studies should be extended to further binders such as fibril-forming polytetrafluoroethylene (PTFE) used for dry processing [72].

4. Conclusion

This study systematically evaluated the densification of separators composed of LPS and HNBR for an application in solid-state batteries. It was found that densification led to increased fragility of the separators, thus complicating their handling during processing and affecting product quality. Consequently, high mechanical instability can result in high rejection rate of defective separator layers and an increased risk of short circuits. Increased brittleness was observed with increasing fabrication pressure likely due to a stronger interlocking of the particles, which decreases the flexibility of the separator. However, an increase in densification temperature results in significant increase in the adhesive strength. A higher layer thickness results in a denser layer for the same fabrication pressure.

Based on FTIR and EDX results, binder migration to the separator surface caused by compaction, resulting in an isolating layer is considered as unlikely. The elastic recovery that might harm the separators microstructure and reduces achievable density after compaction increases with an increase in loading speed and binder content for the tested stress. For the HNBR-LPS separators the measured ionic conductivity is dependent on whether the sample was compacted directly in the cell body used for impedance measurement. This is important to accurately interpret the results obtained by EIS. For LPSCl-HNBR separators however, a deteriorated ionic conductivity after compaction was measured regardless of whether the sample was compacted in the cell body or not. In addition, stress-induced strain that is assumed to increase the ionic conductivity due to the introduction of lattice defects in the electrolyte is reduced with an increase in the binder amount. Based on these results, low binder content for separator production is recommended in order to minimize the reduction in ionic conductivity.

CRediT authorship contribution statement

Carina Amata Heck: Writing – original draft, Visualization, Validation, Project administration, Methodology, Investigation, Formal analysis, Data curation, Conceptualization. **Duc Hien Nguyen:** Writing – original draft, Methodology, Investigation, Formal analysis, Data curation. **Lars Bröcker:** Writing – original draft, Methodology, Investigation, Data curation. **Martin Alexander Lange:** Writing – original draft, Methodology, Investigation, Formal analysis, Data curation. **Vasiliki Faka:** Writing – original draft, Methodology, Investigation, Formal analysis, Data curation. **Alexander Diener:** Writing – review & editing, Validation, Methodology. **Jeff Bastian Wongso Wijaya:** Writing – original draft, Methodology, Investigation. **Lennart Blume:** Writing – review & editing, Validation, Data curation. **Wolfgang G. Zeier:** Writing – review & editing, Supervision, Funding acquisition. **Bettina V. Lotsch:** Writing – review & editing, Supervision, Funding acquisition. **Arno Kwade:** Writing – review & editing, Supervision, Funding acquisition. **Peter Michalowski:** Writing – review & editing, Supervision, Funding acquisition.

Declaration of competing interest

The authors declare that they have no known competing financial interests or personal relationships that could have appeared to influence the work reported in this paper. The authors declare the use of AI tools during the manuscript preparation.

Acknowledgement

This research was funded by the Deutsche Forschungsgemeinschaft (funding code: 514726960 and 459785385) and the German Federal Ministry of Education and Research (BiSSFest, funding code: 403XP0412A; MPI-FestBatt II, funding code: 03XP0430B). We also gratefully thank Jakob Graf-Schlenkrich for the EDX measurements, as well as Stephanie Michel and Achim Overbeck for the nanoindentation measurements. We thank Anne-Katrin Landa for the experimental support, as well as Alexander Schoo, Kevin Voges and Jeroen Volbeda for the scientific discussions.

Appendix A. Supplementary data

Supplementary data to this article can be found online at https://doi.org/10.1016/j.est.2025.120084.

Data availability

Data will be made available on request.

References

[1] J. Janek, W.G. Zeier, A solid future for battery development, Nat. Energy 1 (2016) 1–4, https://doi.org/10.1038/nenergy.2016.141.
[2] M. Batzer, C. Heck, P. Michalowski, A. Kwade, Current status of formulations and scalable processes for producing sulfidic solid-state batteries, Batteries Supercaps 5 (2022) e202200328, https://doi.org/10.1002/batt.202200328.
[3] J. Janek, W.G. Zeier, Challenges in speeding up solid-state battery development, Nat. Energy 8 (2023) 230–240, https://doi.org/10.1038/s41560-023-01208-9.
[4] Z. Yang, W. Wu, M. Duan, S. Chen, M. Liu, J. Liu, T. Huang, H. Liu, Strategies for advanced solid electrolytes toward efficient lithium-ion conduction in all-solid-state lithium metal batteries, ACS Appl. Mater. Interfaces 17 (2025) 22184–22209, https://doi.org/10.1021/acsami.4c23123.
[5] Z. Liu, W. Fu, E.A. Payzant, X. Yu, Z. Wu, N.J. Dudney, J. Kiggans, K. Hong, A. J. Rondinone, C. Liang, Anomalous high ionic conductivity of nanoporous β-Li3PS4, J. Am. Chem. Soc. 135 (2013) 975–978, https://doi.org/10.1021/ja3110895.
[6] F. Marchini, B. Porcheron, G. Rousse, L. Albero Blanquer, L. Droguet, D. Foix, T. Koç, M. Deschamps, J.M. Tarascon, The hidden side of nanoporous β-Li 3 PS 4 solid electrolyte, Adv. Energy Mater. 11 (2021) 2101111, https://doi.org/10.1002/aenm.202101111.
[7] K. Homma, M. Yonemura, T. Kobayashi, M. Nagao, M. Hirayama, R. Kanno, Crystal structure and phase transitions of the lithium ionic conductor Li3PS4, Solid State Ion. 182 (2011) 53–58, https://doi.org/10.1016/j.ssi.2010.10.001.
[8] L.L. Baranowski, C.M. Heveran, V.L. Ferguson, C.R. Stoldt, Multi-scale mechanical behavior of the Li3PS4 solid-phase electrolyte, ACS Appl. Mater. Interfaces 8 (2016) 29573–29579, https://doi.org/10.1021/acsami.6b06612.
[9] Y. Yang, Q. Wu, Y. Cui, Y. Chen, S. Shi, R.-Z. Wang, H. Yan, Elastic properties, defect thermodynamics, electrochemical window, phase stability, and Li(+) mobility of Li3PS4: Insights from first-principles calculations, ACS Appl. Mater. Interfaces 8 (2016) 25229–25242, https://doi.org/10.1021/acsami.6b06754.
[10] A. Tron, R. Hamid, N. Zhang, A. Paolella, P. Wulfert-Holzmann, V. Kolotygin, P. López-Aranguren, A. Beutl, Film processing of Li6PS5Cl electrolyte using different binders and their combinations, J. Energy Storage 66 (2023) 107480, https://doi.org/10.1016/j.est.2023.107480.
[11] J. Liu, J. Sun, Z. Zhang, H. Yang, X. Nie, One-step synthesis of end-functionalized hydrogenated nitrile-butadiene rubber by combining the functional metathesis with hydrogenation, ChemistryOpen 9 (2020) 374–380, https://doi.org/10.1002/open.201900369.
[12] J. Schnell, T. Günther, T. Knoche, C. Vieider, L. Köhler, A. Just, M. Keller, S. Passerini, G. Reinhart, All-solid-state lithium-ion and lithium metal batteries – paving the way to large-scale production, J. Power Sources 382 (2018) 160–175, https://doi.org/10.1016/j.jpowsour.2018.02.062.
[13] T. Scharmann, C. Özcelikman, D.M. Nguyen, C.A. Heck, C. Wacker, P. Michalowski, A. Kwade, K. Dröder, Quantification of hydrogen sulfide development during the production of all-solid-state batteries with argyrodite sulfide-based separators, ACS Appl. Energy Mater. 7 (2024) 1261–1269, https://doi.org/10.1021/acsaem.3c02888.
[14] M. Batzer, K. Voges, W. Wang, P. Michalowski, A. Kwade, Systematic evaluation of materials and recipe for scalable processing of sulfide-based solid-state batteries, Mater. Today Commun. 30 (2022) 103189, https://doi.org/10.1016/j.mtcomm.2022.103189.
[15] C. Heck, T. Scharmann, M. Osenberg, A. Diener, I. Manke, P. Michalowski, A. Kwade, Opportunities and challenges of calendering sulfide-based separators for solid-state batteries, Batteries Supercaps 7 (2024) e202300487, https://doi.org/10.1002/batt.202300487.
[16] C. Singer, S. Schmalzbauer, R. Daub, Influence of the slurry composition on thin-film components for the wet coating process of sulfide-based all-solid-state batteries, J. Energy Storage 68 (2023) 107703, https://doi.org/10.1016/j.est.2023.107703.
[17] R. Koerver, I. Aygün, T. Leichtweiß, C. Dietrich, W. Zhang, J.O. Binder, P. Hartmann, W.G. Zeier, J. Janek, Capacity fade in solid-state batteries: interphase formation and chemomechanical processes in nickel-rich layered oxide cathodes and Lithium thiophosphate solid electrolytes, Chem. Mater. 29 (2017) 5574–5582, https://doi.org/10.1021/acs.chemmater.7b00931.
[18] Y.-G. Lee, S. Fujiki, C. Jung, N. Suzuki, N. Yashiro, R. Omoda, D.-S. Ko, T. Shiratsuchi, T. Sugimoto, S. Ryu, J.H. Ku, T. Watanabe, Y. Park, Y. Aihara, D. Im, I.T. Han, High-energy long-cycling all-solid-state lithium metal batteries enabled by silver–carbon composite anodes, Nat. Energy 5 (2020) 299–308, https://doi.org/10.1038/s41560-020-0575-z.
[19] S. Ito, S. Fujiki, T. Yamada, Y. Aihara, Y. Park, T.Y. Kim, S.-W. Baek, J.-M. Lee, S. Doo, N. Machida, A rocking chair type all-solid-state lithium ion battery adopting Li2O–ZrO2 coated LiNi0.8Co0.15Al0.05O2 and a sulfide based electrolyte, J. Power Sources 248 (2014) 943–950, https://doi.org/10.1016/j.jpowsour.2013.10.005.
[20] M. Grandjean, M. Perrey, X. Randrema, J. Laurier, P. Chenevier, C. Haon, S. Liatard, Low pressure cycling of solid state Li-ion pouch cells based on NMC – Sulfide – Nanosilicon chemistry, J. Power Sources 585 (2023) 233646, https://doi.org/10.1016/j.jpowsour.2023.233646.
[21] J.-M. Doux, Y. Yang, D.H.S. Tan, H. Nguyen, E.A. Wu, X. Wang, A. Banerjee, Y. S. Meng, Pressure effects on sulfide electrolytes for all solid-state batteries, J. Mater. Chem. A 8 (2020) 5049–5055, https://doi.org/10.1039/C9TA12889A.
[22] S. Randau, D.A. Weber, O. Kötz, R. Koerver, P. Braun, A. Weber, E. Ivers-Tiffée, T. Adermann, J. Kulisch, W.G. Zeier, F.H. Richter, J. Janek, Benchmarking the performance of all-solid-state lithium batteries, Nat. Energy 5 (2020) 259–270, https://doi.org/10.1038/s41560-020-0565-1.
[23] Y.J. Nam, D.Y. Oh, S.H. Jung, Y.S. Jung, Toward practical all-solid-state lithium-ion batteries with high energy density and safety: comparative study for electrodes fabricated by dry- and slurry-mixing processes, J. Power Sources 375 (2018) 93–101, https://doi.org/10.1016/j.jpowsour.2017.11.031.
[24] M. Dixit, C. Beamer, R. Amin, J. Shipley, R. Eklund, N. Muralidharan, L. Lindqvist, A. Fritz, R. Essehli, M. Balasubramanian, I. Belharouak, The role of isostatic pressing in large-scale production of solid-state batteries, ACS Energy Letters 7 (11) (2022) 3936–3946, https://doi.org/10.1021/acsenergylett.2c01936.
[25] M. Dixit, C. Beamer, R. Essehli, A. Bisht, R. Amin, M. Li, J. Sharma, T. Rabe, M. Balasubramanian, I. Belharouak, Isostatic pressing of multilayer pouch cells and its implications for battery manufacturing, Device 2 (2024) 100370, https://doi.org/10.1016/j.device.2024.100370.
[26] S. Kim, Y.A. Chart, S. Narayanan, M. Pasta, Thin solid electrolyte separators for solid-state lithium-sulfur batteries, Nano Lett. 22 (2022) 10176–10183, https://doi.org/10.1021/acs.nanolett.2c04216.
[27] N. Riphaus, P. Strobl, B. Stiaszny, T. Zinkevich, M. Yavuz, J. Schnell, S. Indris, H. A. Gasteiger, S.J. Sedlmaier, Slurry-based processing of solid electrolytes: a comparative binder study, J. Electrochem. Soc. 165 (2018) A3993–A3999, https://doi.org/10.1149/2.0961816jes.
[28] M. Cronau, M. Szabo, C. König, T.B. Wassermann, B. Roling, How to measure a reliable ionic conductivity? The stack pressure dilemma of microcrystalline sulfide-

based solid electrolytes, ACS Energy Lett. 6 (2021) 3072–3077, https://doi.org/10.1021/acsenergylett.1c01299.
[29] C. Schneider, C.P. Schmidt, A. Neumann, M. Clausnitzer, M. Sadowski, S. Harm, C. Meier, T. Danner, K. Albe, A. Latz, W.A. Wall, B.V. Lotsch, Effect of particle size and pressure on the transport properties of the fast ion conductor t -Li 7 SiPS 8, Adv. Energy Mater. 13 (2023) 2203873, https://doi.org/10.1002/aenm.202203873.
[30] H.A. Janssen, Versuche über Getreidedruck in Silozellen, VDI Zeitschrift 39 (1895) 1045.
[31] D.H. Nguyen, M. Osenberg, C. Schneider, J. Moosmann, F. Beckmann, I. Manke, B. V. Lotsch, Effect of stack pressure on the microstructure and ionic conductivity of the slurry-processed solid electrolyte Li7SiPS8, Adv. Mater. Interfaces 12 (2025) e00845, https://doi.org/10.1002/admi.202500845.
[32] C. Sedlmeier, T. Kutsch, R. Schuster, L. Hartmann, R. Bublitz, M. Tominac, M. Bohn, H.A. Gasteiger, From powder to sheets: a comparative electrolyte study for slurry-based processed solid electrolyte/binder-sheets as separators in all-solid-state batteries, J. Electrochem. Soc. 169 (2022) 70508, https://doi.org/10.1149/1945-7111/ac7e76.
[33] A.K. Schomberg, A. Diener, I. Wünsch, J.H. Finke, A. Kwade, The use of X-ray microtomography to investigate the microstructure of pharmaceutical tablets: potentials and comparison to common physical methods, Int. J. Pharm.: X 3 (2021) 100090, https://doi.org/10.1016/j.ijpx.2021.100090.
[34] R. Garcia-Mendez, J.G. Smith, J.C. Neuefeind, D.J. Siegel, J. Sakamoto, Correlating macro and atomic structure with elastic properties and ionic transport of glassy Li2S-P2S5 (LPS) solid electrolyte for solid-state Li metal batteries, Adv. Energy Mater. 10 (2020) 2000335, https://doi.org/10.1002/aenm.202000335.
[35] W. Haselrieder, S. Ivanov, D.K. Christen, H. Bockholt, A. Kwade, Impact of the calendering process on the interfacial structure and the related electrochemical performance of secondary lithium-ion batteries, ECS Trans. 50 (2013) 59–70, https://doi.org/10.1149/05026.0059ecst.
[36] W. Haselrieder, B. Westphal, H. Bockholt, A. Diener, S. Höft, A. Kwade, Measuring the coating adhesion strength of electrodes for lithium-ion batteries, Int. J. Adhes. Adhes. 60 (2015) 1–8, https://doi.org/10.1016/j.ijadhadh.2015.03.002.
[37] L. Froboese, P. Titscher, B. Westphal, W. Haselrieder, A. Kwade, Mercury intrusion for ion- and conversion-based battery electrodes – structure and diffusion coefficient determination, Mater. Charact. 133 (2017) 102–111, https://doi.org/10.1016/j.matchar.2017.09.002.
[38] M. Batzer, D. Gundlach, P. Michalowski, A. Kwade, Scalable production of separator and cathode suspensions via extrusion for sulfidic solid-state batteries, ChemElectroChem 10 (2023) e202300452, https://doi.org/10.1002/celc.202300452.
[39] J. Huang, N.P. Sullivan, A. Zakutayev, R. O'Hayre, How reliable is distribution of relaxation times (DRT) analysis? A dual regression-classification perspective on DRT estimation, interpretation, and accuracy, Electrochim. Acta 443 (2023) 141879, https://doi.org/10.1016/j.electacta.2023.141879.
[40] A.A. Coelho, TOPAS and TOPAS-academic an optimization program integrating computer algebra and crystallographic objects written in C++, J. Appl. Cryst. 51 (2018) 210–218, https://doi.org/10.1107/S1600576718000183.
[41] S. Christensen, N. Bindzus, M. Sist, M. Takata, B.B. Iversen, Structural disorder, anisotropic micro-strain and cation vacancies in thermo-electric lead chalcogenides, Phys. Chem. Chem. Phys. 18 (2016) 15874–15883, https://doi.org/10.1039/c6cp01730d.
[42] P.W. Stephens, Phenomenological model of anisotropic peak broadening in powder diffraction, Appl. Crystallogr. 32 (2) (1999) 281–289.
[43] B.H. Toby, R.B. von Dreele, GSAS-II the genesis of a modern open-source all purpose crystallography software package, J. Appl. Cryst. 46 (2013) 544–549, https://doi.org/10.1107/S0021889813003531.
[44] F.P. McGrogan, T. Swamy, S.R. Bishop, E. Eggleton, L. Porz, X. Chen, Y.-M. Chiang, K.J. van Vliet, Compliant yet brittle mechanical behavior of Li2S-P2S5 lithium-ion-conducting solid electrolyte, Adv. Energy Mater. 7 (2017) 1602011, https://doi.org/10.1002/aenm.201602011.
[45] C. Meyer, M. Weyhe, W. Haselrieder, A. Kwade, Heated calendering of cathodes for Lithium-ion batteries with varied carbon black and binder contents, Energy Technol. 8 (2020) 1900175, https://doi.org/10.1002/ente.201900175.
[46] M.O. Vityk, R.J. Bodnar, Statistical microthermometry of synthetic fluid inclusions in quartz during decompression reequilibration, Contrib. Mineral. Petrol. 132 (1998) 146–162.
[47] D.K. Singh, A. Henss, B. Mogwitz, A. Gautam, J. Horn, T. Krauskopf, S. Burkhardt, J. Sann, F.H. Richter, J. Janek, Li6PS5Cl microstructure and influence on dendrite growth in solid-state batteries with lithium metal anode, Cell Rep. Phys. Sci. 3 (2022) 101043, https://doi.org/10.1016/j.xcrp.2022.101043.
[48] H. Chen, H. Zhang, Y. Zhou, J. Chen, X. Huang, B. Tian, Structure-conduction correlations in a chlorine-rich superionic lithium-argyrodite solid electrolyte: a DRT analysis, J. Power Sources 583 (2023) 233579, https://doi.org/10.1016/j.jpowsour.2023.233579.
[49] J. Spychala, C. Mandl, K. Hogrefe, H.M.R. Wilkening, B. Gadermaier, Morphology-dependent Li+ ion dynamics in X-ray amorphous and crystalline Li3PS4 prepared by solvent-assisted synthesis, Dalton Trans. 54 (2025) 2283–2293, https://doi.org/10.1039/D4DT02636E.
[50] H.-J. Deiseroth, S.-T. Kong, H. Eckert, J. Vannahme, C. Reiner, T. Zaiß, M. Schlosser, Li6PS5X: a class of crystalline Li-rich solids with an unusually high Li + mobility, Angew. Chem. 120 (2008) 767–770, https://doi.org/10.1002/ange.200703900.
[51] K. Yamamoto, S. Yang, M. Takahashi, K. Ohara, T. Uchiyama, T. Watanabe, A. Sakuda, A. Hayashi, M. Tatsumisago, H. Muto, A. Matsuda, Y. Uchimoto, High ionic conductivity of liquid-phase-synthesized Li3PS4 solid electrolyte, comparable to that obtained via ball milling, ACS Appl. Energy Mater. 4 (2021) 2275–2281, https://doi.org/10.1021/acsaem.0c02771.
[52] A. Ito, T. Kimura, A. Sakuda, M. Tatsumisago, A. Hayashi, Liquid-phase synthesis of Li3PS4 solid electrolyte using ethylenediamine, J. Sol-Gel Sci. Technol. 101 (2022) 2–7, https://doi.org/10.1007/s10971-021-05524-y.
[53] V. Faka, M.T. Agne, M.A. Lange, D. Daisenberger, B. Wankmiller, S. Schwarzmüller, H. Huppertz, O. Maus, B. Helm, T. Böger, J. Hartel, J.M. Gerdes, J.J. Molaison, G. Kieslich, M.R. Hansen, W.G. Zeier, Pressure-induced dislocations and their influence on ionic transport in Li+-conducting argyrodites, J. Am. Chem. Soc. 146 (2024) 1710–1721, https://doi.org/10.1021/jacs.3c12323.
[54] C. Meyer, H. Bockholt, W. Haselrieder, A. Kwade, Characterization of the calendering process for compaction of electrodes for lithium-ion batteries, J. Mater. Process. Technol. 249 (2017) 172–178, https://doi.org/10.1016/j.jmatprotec.2017.05.031.
[55] R.W. Heckel, Density-pressure relationship in powder compaction, Trans. Metall. Soc. AIME 221 (1961) 671–675.
[56] A. Diener, S. Ivanov, W. Haselrieder, A. Kwade, Evaluation of deformation behavior and fast elastic recovery of lithium-ion battery cathodes via direct roll-gap detection during calendering, Energy Technol. 10 (2022) 2101033, https://doi.org/10.1002/ente.202101033.
[57] C. Meyer, M. Kosfeld, W. Haselrieder, A. Kwade, Process modeling of the electrode calendering of lithium-ion batteries regarding variation of cathode active materials and mass loadings, J. Energy Storage 18 (2018) 371–379, https://doi.org/10.1016/j.est.2018.05.018.
[58] C. Sun, D.J. Grant, Influence of elastic deformation of particles on Heckel analysis, Pharm. Dev. Technol. 6 (2001) 193–200, https://doi.org/10.1081/PDT-100000738.
[59] C.A. Heck, F. Huttner, J.K. Mayer, O. Fromm, M. Börner, T. Heckmann, P. Scharfer, W. Schabel, M. Winter, A. Kwade, Production of nickel-rich cathodes for lithium-ion batteries from lab to pilot scale under investigation of the process atmosphere, Energy Technol. 11 (2023) 2200945, https://doi.org/10.1002/ente.202200945.
[60] M. Yamamoto, M. Takahashi, Y. Terauchi, Y. Kobayashi, S. Ikeda, A. Sakuda, Fabrication of composite positive electrode sheet with high active material content and effect of fabrication pressure for all-solid-state battery, J. Ceram. Soc. Jpn. 125 (2017) 391–395, https://doi.org/10.2109/jcersj2.16321.
[61] A. Ohashi, M. Kodama, S. Xueying, S. Hori, K. Suzuki, R. Kanno, S. Hirai, Stress distribution in the composite electrodes of sulfide all-solid-state lithium-ion batteries, J. Power Sources 470 (2020) 228437, https://doi.org/10.1016/j.jpowsour.2020.228437.
[62] F. Huttner, A. Diener, T. Heckmann, J.C. Eser, T. Abali, J.K. Mayer, P. Scharfer, W. Schabel, A. Kwade, Increased moisture uptake of NCM622 cathodes after calendering due to particle breakage, J. Electrochem. Soc. 168 (2021) 90539, https://doi.org/10.1149/1945-7111/ac24bb.
[63] K. Schönert, Advances in comminution fundamentals and impacts on technology, Aufarbeitungstechnik 32 (1991) 487–494.
[64] S. Breitung-Faes, A. Kwade, Prediction of energy effective grinding conditions, Miner. Eng. 43–44 (2013) 36–43, https://doi.org/10.1016/j.mineng.2012.07.015.
[65] H. Rumpf, Die Einzelkornzerkleinerung als Grundlage einer technischen Zerkleinerungswissenschaft, Chem. Ing. Tech. 37 (1965) 187–202, https://doi.org/10.1002/cite.330370303.
[66] L.H. Adem, B.N. Olana, B.W. Taklu, B.D. Dandena, G.G. Serbessa, B.-J. Hwang, S. D. Lin, In situ DRIFTS analysis of the evolution of surface species over Li6PS5Cl solid state electrolyte during moisture-induced degradation and during heat treatment, Electrochim. Acta 498 (2024) 144622, https://doi.org/10.1016/j.electacta.2024.144622.
[67] L. Wang, Y. Ni, X. Qi, L. Zhang, D. Yue, Synthesis of low temperature resistant hydrogenated nitrile rubber based on esterification reaction, Polymers 13 (2021) 4096, https://doi.org/10.3390/polym13234096.
[68] V.P. Tolstoy, I.V. Chernyshova, V.A. Skryshevsky (Eds.), Handbook of Infrared Spectra of Ultrathin Films, John Wiley & Sons, 2003.
[69] L. Kang, M. Zhou, J. Yao, Z. Lin, Y. Wu, C. Chen, Metal thiophosphates with good mid-infrared nonlinear optical performances: a first-principles prediction and analysis, J. Am. Chem. Soc. 137 (2015) 13049–13059, https://doi.org/10.1021/jacs.5b07920.
[70] M. Maroufkhani, A. Katbab, W. Liu, J. Zhang, Polylactide (PLA) and acrylonitrile butadiene rubber (NBR) blends: the effect of ACN content on morphology, compatibility and mechanical properties, Polymer 115 (2017) 37–44, https://doi.org/10.1016/j.polymer.2017.03.025.
[71] J. Choi, J.Y. Kim, S.H. Kang, D.O. Shin, M.J. Lee, Y.-G. Lee, Revealing interfacial parasitic reactions of nitrile rubber binders in all-solid-state lithium batteries, J. Mater. Chem. A 12 (2024) 6426–6437, https://doi.org/10.1039/d3ta06853f.
[72] M. Rosner, S. Cangaz, F. Hippauf, S. Dörfler, B. Aktekin, T. Meyer, A. Henss, T. Abendroth, H. Althues, J. Janek, S. Kaskel, Analysis of the electrochemical stability of sulfide solid electrolyte dry films for improved dry-processed solid-state batteries, Adv. Funct. Mater. e18517 (2025), https://doi.org/10.1002/adfm.202518517.